

# MEASURING THE LUMINOSITY AND VIRIAL BLACK HOLE MASS DEPENDENCE OF QUASAR-GALAXY CLUSTERING AT $z \sim 0.8$

ALEX G. KROLEWSKI, DANIEL J. EISENSTEIN

Harvard-Smithsonian Center for Astrophysics, 60 Garden Street, Cambridge, MA 02138, USA

*Draft version December 2, 2018*

## ABSTRACT

We study the dependence of quasar clustering on quasar luminosity and black hole mass by measuring the angular overdensity of photometrically selected galaxies imaged by WISE about  $z \sim 0.8$  quasars from SDSS. By measuring the quasar-galaxy cross-correlation function and using photometrically selected galaxies, we achieve a higher density of tracer objects and a more sensitive detection of clustering than measurements of the quasar autocorrelation function. We test models of quasar formation and evolution by measuring the luminosity dependence of clustering amplitude. We find a significant overdensity of WISE galaxies about  $z \sim 0.8$  quasars at  $0.2\text{--}6.4 h^{-1}$  Mpc in projected comoving separation. We find no appreciable increase in clustering amplitude with quasar luminosity across a decade in luminosity, and a power-law fit between luminosity and clustering amplitude gives an exponent of  $-0.01 \pm 0.06$  ( $1 \sigma$  errorbar). We also fail to find a significant relationship between clustering amplitude and black hole mass, although our dynamic range in true mass is suppressed due to the large uncertainties in virial black hole mass estimates. Our results indicate that a small range in host dark matter halo mass maps to a large range in quasar luminosity.

*Subject headings:* quasars: general, galaxies: active, large-scale structure of universe

## 1. BACKGROUND

Direct observations have recently confirmed that nearly every nearby elliptical galaxy or spiral bulge hosts a central supermassive black hole (Kormendy & Richstone 1995). Further studies have shown that black hole properties are tightly related to the macroscopic properties of the host galaxy. Black hole mass is closely tied to both the stellar velocity dispersion (Gebhardt et al. 2000; Ferrarese & Merritt 2000) and the mass of the associated spheroid (e.g. spiral bulge or elliptical galaxy; Marconi & Hunt 2003; Magorrian et al. 1998). Both the velocity dispersion and spheroid mass are related to the mass of the host dark matter halo (Ferrarese 2002). These relationships provide evidence for a link between black hole and host galaxy evolution (Silk & Rees 1998; Hopkins et al. 2006).

Local supermassive black holes are relics of past quasar activity (Soltan 1982). Quasars are an important stage in the coevolution of a black hole and its host galaxy. Quasar activity is associated with massive, disruptive flows of gas into the center of the galaxy, and simulations predict that quasar activity suppresses star formation, leading to a link between black hole mass and host spheroid mass (Di Matteo et al. 2005).

However, the details of quasar formation and evolution are not fully known. Many different models have been proposed to explain quasar activity, ranging in sophistication from numerical simulations of quasar activity tracking gas hydrodynamics (Hopkins et al. 2008; Degraf et al. 2011; Thacker et al. 2009; Chatterjee et al. 2012) to semi-analytical methods tracking only dark matter halos (Kauffmann & Haehnelt 2000, 2002; Bonoli et al. 2009; Fanidakis et al. 2012) to scaling relations with no preferences for the underlying physics (Conroy & White 2013; Lidz et al. 2006; Croton 2009; Shen 2009; Booth & Schaye

2010). A brief, comprehensive, and useful overview of various quasar models can be found in Appendix B of White et al. (2012). In this paper, we consider the differences between low and high luminosity quasars, and between low and high mass black holes. Specifically, we study the relationships between luminosity and host halo mass and between black hole mass and host halo mass by measuring quasar clustering.

Quasar clustering is a valuable tool for exploring quasar properties and evolution. Quasar clustering is often measured using the linear quasar bias  $b_Q$ , defined by

$$\xi_Q = b_Q^2 \xi_{\text{matter}} \quad (1)$$

where  $\xi_Q$  is the quasar autocorrelation function and  $\xi_{\text{matter}}$  is the correlation function of the linear-regime matter field. The bias is then converted to the host halo mass using analytic formulas tested against  $N$ -body simulations (Cole & Kaiser 1989; Mo & White 1996; Sheth et al. 2001), which predict that at fixed redshift the halo mass is a monotonically increasing function of bias. Measurements of the luminosity dependence of quasar clustering allow estimation of the slope and scatter of the relationship between luminosity and host halo mass. The halo mass-luminosity relationship arises from the combination of a black hole mass-luminosity relationship and a halo mass-black hole mass relationship. By also measuring the black hole mass dependence of clustering, we can separate the contributions of the black hole mass-luminosity relationship from the halo mass-black hole mass relationship.

The quasar lifetime can be determined from measurements of the quasar bias (Cole & Kaiser 1989; Haiman & Hui 2001; Martini & Weinberg 2001). If quasars are long-lived, then most of the quasars in the universe are actively accreting and quasars are rare, whereas if quasars are short-lived, there are many unobserved dor-

mant quasars for each observed active quasar and quasars are common. Since high mass, highly biased halos are rare (Press & Schechter 1974) a highly biased quasar population implies a long lifetime. The conversion between bias and lifetime assumes that luminosity is a monotonic function of halo mass with no scatter. If there is scatter in the luminosity-halo mass relationship, the lifetime is greater than for the no-scatter case (Martini & Weinberg 2001). Thus, measurements of the luminosity dependence of quasar clustering allow for joint determination of the quasar lifetime and the scatter in the luminosity-halo mass relationship (Shankar et al. 2010). The analysis of Martini & Weinberg (2001) and Haiman & Hui (2001) assumed that the quasar lightcurve is a step function, either “on” or “off” at any given time. More sophisticated models of the quasar lightcurve have been proposed (e.g. Kauffmann & Haehnelt 2002; Lidz et al. 2006), leading to predictions of luminosity or redshift-dependent lifetimes. In principle, measurements of the luminosity dependence of clustering can help distinguish between different models of the quasar lightcurve.

Large surveys such as the Sloan Digital Sky Survey (York et al. 2000) and the 2dF QSO Redshift Survey (Croom et al. 2004) provide the large samples necessary to study the luminosity dependence of quasar clustering. Early studies measured the luminosity dependence of the real-space and redshift-space autocorrelation function using spectroscopically selected quasars: Croom et al. (2005) found no luminosity dependence of the redshift-space clustering strength of 2dF quasars at  $0.5 < z < 2.5$ , and Porciani & Norberg (2006) found no luminosity dependence on real-space clustering strength for 2dF quasars at  $0.8 < z < 1.3$  and only marginal evidence at  $1.3 < z < 2.1$ . More recently, Shanks et al. (2011) found no luminosity dependence on clustering strength at  $z = 1.4$  using quasar autocorrelation measurements from 2QZ, 2SLAQ, and SDSS, and White et al. (2012) found no luminosity dependence on redshift-space clustering strength for SDSS quasars at  $z = 2.4$ . Due to the low space density of spectroscopically detected quasars, these studies generally suffer from large error bars. One way to obtain smaller error bars is to measure the autocorrelation function of photometrically selected quasars. Myers et al. (2007) measured the autocorrelation of 300,000 photometric quasars from SDSS and found no luminosity dependence of quasar bias at photometric redshifts  $z = 0.85$ ,  $z = 1.44$ , and  $z = 1.92$ .

Another approach is to measure the cross-correlation of galaxies about quasars. Since galaxies have a much higher spatial density than quasars, cross-correlations can achieve lower error bars than autocorrelations (as suggested by Kauffmann & Haehnelt 2002). Early quasar-galaxy cross-correlations used small samples and thus had large error bars. Adelberger & Steidel (2005), measuring the cross-correlation of quasars at  $2 < z < 3$  with Lyman-break galaxies, found no luminosity dependence across 4 decades in quasar luminosity, but urged caution in interpretation of their result due to large error bars. Similarly, Coil et al. (2007) also found no luminosity dependence on quasar-galaxy clustering at  $z \approx 1$ , but again with relatively large error bars. More recent studies found little evidence for luminosity-dependent clustering with larger samples and smaller error bars (da Ángela

et al. 2008; Shen et al. 2009; Mountrichas et al. 2009; Shirasaki et al. 2011; Shen et al. 2013), although Shen et al. (2009) did find an increase in bias for the most luminous 10% of quasars.

Some studies used photometrically detected galaxies rather than spectroscopic galaxies to increase the size of the tracer population and further decrease their statistical errors. Padmanabhan et al. (2009) found no luminosity evolution in the cross-correlation between SDSS DR5 quasars and luminous red galaxies with photometric redshifts at  $0.2 < z < 0.6$ . Zhang et al. (2013) found no luminosity dependence in the cross-correlation between DR5 quasars and photometrically detected galaxies from SDSS Stripe 82.

While most studies focused on the optical luminosity dependence of quasar clustering, other studies measured the luminosity dependence at different wavelengths. Hickox et al. (2009) found significant variation in clustering strength between radio, X-ray, and infrared selected AGNs. Using X-ray selected quasars from ROSAT, Krumpel et al. (2012) found a  $2\sigma$  dependence of clustering strength on X-ray luminosity, and attributed the discrepancy between measurements of the optical luminosity dependence and measurements of the X-ray luminosity dependence to the much larger dynamic range in X-ray luminosity.

Fewer studies have attempted to measure black hole mass dependent clustering due to the much higher uncertainties of black hole mass estimates. Black hole masses can be estimated from single-epoch spectroscopy using continuum luminosity and emission line width (Vestergaard & Peterson 2006) with uncertainties up to 0.5 decades for individual objects (Shen 2013). Throughout this paper, we refer to these estimates as “virial black hole masses” to emphasize the large associated uncertainties.

Using the same sample as Croom et al. (2005), Fine et al. (2006) constructed composite spectra for each of 10 bins in redshift and measured the virial mass for each composite spectrum. They found a  $M_{\text{BH}} - M_{\text{DMH}}$  relationship in good agreement with the models of Ferrarese (2002), although with substantial uncertainties in the slope and zeropoint of the relation due to both the small dynamic range in virial mass and the Malmquist bias arising from the 2QZ flux limit. Other studies measured the evolution of clustering with virial mass at fixed redshift: Shen et al. (2009) found no dependence of quasar clustering on virial mass using two bins in virial mass, and Zhang et al. (2013) found a  $1-2\sigma$  difference in clustering strength between two bins in virial mass. However, these studies were hampered by a small number of bins and a small dynamic range in virial mass, implying an even smaller range in true mass due to the uncertainty in the virial masses (Shen et al. 2009). Komiya et al. (2013) studied the virial mass dependence of AGN clustering across a wide range of redshifts ( $0.1 < z < 1.0$ ) and luminosities, combining samples from SDSS DR4 and DR7 to measure clustering across 2 decades in virial mass. They found a significant trend of increasing clustering strength with increasing virial hole mass across 4 bins in virial mass, with a  $2-3\sigma$  difference in clustering strength between the highest and lowest mass groups.

In this study, we measure the angular overdensity of photometric galaxies about spectroscopic quasars to obtain as numerous a tracer population as possible, min-

imizing statistical errors. We measure the luminosity and black hole mass dependence of the quasar-galaxy clustering amplitude at  $0.65 < z < 0.9$ , using a galaxy sample drawn from the Wide-Field Infrared Survey Explorer (Wright et al. 2010) and quasar samples from the SDSS DR7 (Shen et al. 2011) and DR10 quasar catalogs (Pâris et al. 2014). Because the WISE galaxies lack spectroscopic redshifts, we measure the angular correlation using only the galaxy and quasar positions on the sky. Since emission from galaxies at  $z \sim 0.8$  peaks in the near-infrared, we expect that WISE selection will maximize the size of our tracer population.

In this paper we begin by discussing the quasar and galaxy samples and their selection criteria (Section 2). Then we present the angular clustering measurement (Section 3) and find the dependence upon luminosity and virial black hole mass (Section 4). Finally we discuss the significance of these results and compare them to previous studies (Section 5). Throughout this paper, we use a  $\Lambda$ CDM cosmology with  $h = 0.7$ ,  $\Omega_\Lambda = 0.7$  and  $\Omega_m = 0.3$  (Spergel et al. 2003), matching the cosmology used to construct the DR7 and DR10 quasar catalogs. When computing the power spectrum of the linear-regime matter field, we use the transfer function of Eisenstein & Hu (1998) and  $\Omega_b = 0.044$ ,  $T_{\text{CMB}} = 2.726$  K,  $N_\nu = 3$ , and  $n_s = 0.93$  (Spergel et al. 2003). All distances are measured in comoving  $h^{-1}$  Mpc.

## 2. QUASAR AND GALAXY SAMPLE SELECTION

We use a color-selected sample of  $z \gtrsim 0.6$  galaxies from WISE and  $0.65 < z < 0.9$  quasars from the SDSS DR7 and DR10 quasar catalogs to measure quasar-galaxy clustering. The galaxy sample was chosen to maximize purity rather than completeness, allowing us to obtain a high signal-to-noise measurement of quasar-galaxy clustering. Galaxy colors are measured by comparing SDSS and WISE imaging.

### 2.1. Galaxy selection: SDSS and WISE

The Wide-Field Infrared Survey Explorer is a satellite that mapped the entire sky at 3.4, 4.6, 12 and 22  $\mu\text{m}$  at sensitivities corresponding to Vega magnitudes of 16.5, 15.5, 11.2, and 7.9 in unconfused regions of the sky (Wright et al. 2010). WISE collected at least 12 exposures at each point on the sky, with coverage depth increasing rapidly towards the Ecliptic poles due to the WISE scan strategy. We select objects from the All-Sky Data Release Source Catalog, which contains 563 million objects that are not flagged as an image artifact and have both  $\text{SNR} > 5$  in at least one band and detections in at least 5 single-band exposures. The All-Sky Data Release uses imaging taken from January to August 2010, and extensive documentation can be found at <http://wise2.ipac.caltech.edu/docs/release/allsky/>. We use imaging from the  $W1$  band at 3.4  $\mu\text{m}$ , which has angular resolution of 6" (Wright et al. 2010). The WISE limiting magnitude varies across the sky, most notably due to increased source confusion at low Galactic latitude<sup>1</sup>. We only consider objects with Galactic latitude  $b > 25^\circ$ ; at these latitudes, the  $W1$

magnitude limit is approximately constant. WISE photometry is given in Vega magnitudes, uncorrected for Galactic dust extinction, which is negligible at 3.4  $\mu\text{m}$ . For sources with  $15.5 < W1 < 16$ , similar in brightness to those selected in our galaxy catalog, the astrometric accuracy of WISE is  $\approx 0.4''$ , as measured by the RMS of the WISE-2MASS positional difference<sup>2</sup>.

The Sloan Digital Sky Survey imaged an area of 14555  $\text{deg}^2$  in 5 filters (*ugriz*; Fukugita et al. 1996), mostly at high Galactic latitude, using a 2.5 m wide-field telescope at Apache Point Observatory in New Mexico (Gunn et al. 2006) and a camera with 30 2048 by 2048 CCDs (Gunn et al. 1998). Imaging data was collected only under photometric conditions (Hogg et al. 2001) and photometry was calibrated to 1% accuracy (Smith et al. 2002; Ivezić et al. 2004; Tucker et al. 2006; Padmanabhan et al. 2008) with negligible spatial variation in photometric calibration (Fukugita et al. 2004). All SDSS magnitudes cited in this paper are corrected for Galactic extinction using the Schlegel-Finkbeiner-Davis dust map (Schlegel et al. 1998) and are reported as *asinh* magnitudes (Lupton et al. 1999) in the AB system (Fukugita et al. 1996). SDSS photometry is 95% complete at  $r = 22$  (Stoughton et al. 2002). Astrometry is typically accurate to 0.1" (Pier et al. 2003), although the photometric data used in this paper (DR8; Aihara et al. 2011b) contain an astrometric calibration error that causes a shift of 0.24" north and 0.05" west over a large region covering most of the survey with declination  $> 41^\circ$  (Aihara et al. 2011a). However, the effect of the astrometry error on our work is negligible.

The SDSS photometric pipeline separates extended sources from point sources based on the difference between the PSF magnitude and a composite model magnitude consisting of a linear combination of de Vaucouleurs and exponential light profiles (Stoughton et al. 2002). Many galaxies at  $z \sim 0.8$  are unresolved, particularly in regions of poor seeing. To eliminate seeing-dependent variations in galaxy sample density, our sample contains point sources as well as extended sources in SDSS imaging. For both point sources and extended sources, we use the best-fit exponential or de Vaucouleurs model magnitudes (Stoughton et al. 2002). We select our objects using the catalogs from the DR8 data sweeps, which contain point sources with at least one extinction-corrected PSF magnitude less than [22.5, 22.5, 22.5, 22, 21.5] (*ugriz*) and extended sources with at least one extinction-corrected model magnitude less than [21, 22, 22, 20.5, 20.1] (*ugriz*) (Blanton et al. 2005).

We use a color cut to ensure that our sample is composed primarily of  $z \gtrsim 0.6$  galaxies. In order to choose an appropriate color cut, we match WISE and SDSS photometry to spectroscopic redshifts for 20,000 galaxies measured by the AGN and Galaxy Evolution Survey (AGES) (Kochanek et al. 2012). To calculate WISE-SDSS colors, we use  $r$  magnitudes in the AB system and  $W1$  magnitudes in the Vega system. Color cuts based on WISE bands alone are inadequate, so instead we select all galaxies with  $r - W1 > 5.5$ . This is a conservative color cut that minimizes the number of stars and low-redshift galaxies in our sample, reducing statistical

<sup>1</sup> See Figure 9 at [http://wise2.ipac.caltech.edu/docs/release/allsky/expsup/sec2\\_2.html](http://wise2.ipac.caltech.edu/docs/release/allsky/expsup/sec2_2.html).

<sup>2</sup> [http://wise2.ipac.caltech.edu/docs/release/allsky/expsup/sec6\\_4.html](http://wise2.ipac.caltech.edu/docs/release/allsky/expsup/sec6_4.html).

uncertainty in our clustering measurement. As Figure 1 shows, the vast majority of the galaxies satisfying our color cut have  $z > 0.65$ . However, many galaxies with  $z > 0.65$  have  $r - W1 < 5.5$ , particularly blue galaxies with  $0.6 < z < 0.8$ . In this study, we assume that the luminosity and virial mass dependence of clustering is the same for red galaxies as for blue galaxies.

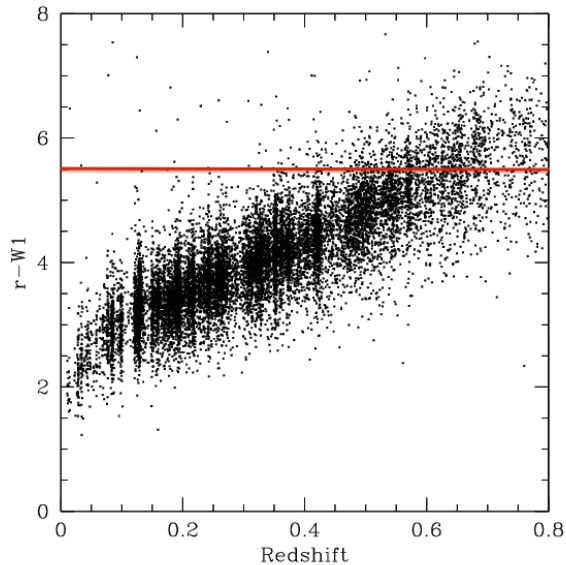


**Figure 1.** Redshift vs. extinction-corrected color for a sample of galaxies from the AGES survey. Note that  $r$  is reported in AB magnitudes while  $W1$  is reported in Vega magnitudes. All points above the red line would be included by our color cut. Since most of these galaxies have  $z > 0.65$ , our color cut removes many contaminating  $z < 0.6$  galaxies. Almost all of the severe deviations from the linear trend are objects with spurious colors and should be ignored.

We begin by choosing WISE detections with  $14 < W1 < 16.5$ ,  $W1 \text{ SNR} > 5$  and Galactic latitude  $b > 25^\circ$ . Less than 0.1% of the BOSS luminous red galaxies with  $0.65 < z < 0.9$  have  $W1 < 14^3$ , so cutting objects with  $W1 < 14$  reduces stellar contamination without removing  $z \gtrsim 0.6$  galaxies. We also remove potentially variable, saturated, or contaminated detections and detections that were deblended more than once ( $W1\text{SAT} > 0$ ,  $W1\text{CC\_MAP} > 0$ ,  $\text{VAR\_FLG} > 5$ , and  $\text{NB} > 2^4$ ). Since nearly every  $z \gtrsim 0.6$  galaxy is unresolved in WISE imaging, we remove detections that are extended sources in WISE ( $\text{EXT\_FLG} > 0$ ). Last, we remove detections with more than 10% of observations contaminated by scattered moonlight ( $\text{MOON\_LEV} > 1$ ). Since the detections with moonlight contamination are highly clustered due to the WISE moon avoidance maneuvers<sup>5</sup>, we exclude all WISE detections in regions with high moon contamination.

Visual inspection of WISE detections reveals a problem with WISE deblending. About 5–10% of WISE de-

tections within the SDSS imaging footprint but without a matching SDSS detection are blended into bright neighboring detections in WISE imaging (see Figure 2). In many of these cases, SDSS found a bright extended galaxy within  $10''$  of the WISE detection. It appears that the WISE detection should have been matched to the SDSS galaxy, but differences in the WISE and SDSS deblending algorithms caused a spurious offset between the WISE and SDSS positions, large enough so that the two detections could not be matched. The SDSS galaxies are all contaminating  $z < 0.6$  galaxies that should not be included in our sample. Note that we still find many of these deblending problems even when we only consider WISE detections with  $\text{NB} \leq 2$ .

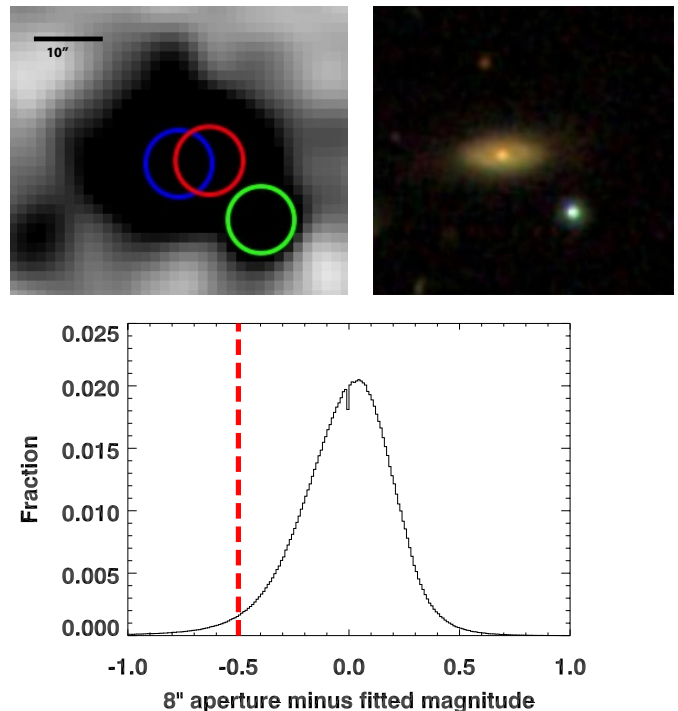


**Figure 2.** *Top:* example of a WISE blending problem in WISE (left) and SDSS (right), located at  $22^{\text{h}}52^{\text{m}}09^{\text{s}}.02, 1^{\circ}38'6.4''$ . The two images cover the same region of the sky. The colored circles on the WISE image are centered on WISE detections; the red circle lacks an SDSS match. It is clear that the red and blue circles are both associated with the bright yellow galaxy at the center of the SDSS image and the red circle is merely an artifact of the WISE deblending process. *Bottom:* Distribution of  $W1$  aperture minus fitted magnitude ( $A - F$ ) for WISE detections included in our sample. The tail on the left results from deblended sources such as those in the top images, which have an extended flux profile despite being classified as point sources. Because these could be contaminating low-redshift objects, we removed all detections with  $A - F < -0.5$ .

In order to remove these detections from our sample, we compare two different measurements of  $W1$  magnitude: one computed by summing all the flux within an  $8.25''$  aperture ( $W1\text{MAG\_2}$ ; referred to as  $A$  for clarity), and the standard Gaussian profile-fitted magnitude measurement ( $W1\text{MPRO}$ ;  $F$  for clarity). We expect detections with blending problems to have unusually extended flux profiles. Since the profile-fitted mag-

<sup>3</sup> These are mostly CMASS galaxies; see White et al. (2011) for the sample selection criteria.

<sup>4</sup> See [http://wise2.ipac.caltech.edu/docs/release/allsky/expsup/sec2\\_2a.html](http://wise2.ipac.caltech.edu/docs/release/allsky/expsup/sec2_2a.html) for definitions.

<sup>5</sup> See [http://wise2.ipac.caltech.edu/docs/release/prelim/expsup/sec3\\_4a.html](http://wise2.ipac.caltech.edu/docs/release/prelim/expsup/sec3_4a.html).

nitudes are largely determined by the central flux, detections with blending problems should have brighter 8.25" aperture magnitudes than profile-fitted magnitudes. Indeed, the distribution of aperture minus fitted magnitudes ( $A - F$ ) has an asymmetrical tail of detections with an extended flux profile (Figure 2). Since the distribution is nearly zero for  $A - F > 0.5$ , we impose a symmetrical cut on the opposite tail and keep only those detections with  $A - F > -0.5$  (Figure 2). Visual inspection of 50 objects with  $A - F < -0.5$  shows that nearly three quarters have blending issues like Figure 2. However, blending issues are very uncommon for  $A - F > -0.5$ . We find that cutting all objects with  $A - F < -0.5$  is more effective at removing deblending problems than cutting all detections that were deblended at least once.

Our galaxy sample consists of all WISE detections meeting the above criteria that have  $r - W1 > 5.5$ . Since SDSS photometry is complete to  $r = 22$  and our sample only includes detections with  $W1 < 16.5$ , WISE detections imaged by SDSS but lacking an SDSS match meet our color cut and are included in our sample. Our galaxy sample consists of two components: WISE-SDSS matches with  $r - W1 > 5.5$  ("matches") and WISE detections located within the SDSS imaging area that do not match an SDSS detection ("non-matches"). In order to determine the SDSS imaging area, we use the SDSS imaging mask of Ho et al. (2012), which is more restrictive than the SDSS imaging footprint: it removes regions with poor seeing, low Galactic latitude, and nearby bright stars, all of which may contaminate clustering measurements. This yields a final area of 6966 deg<sup>2</sup>. We exclude all WISE detections lying outside the SDSS imaging mask of Ho et al. (2012) because we have no information about these objects' WISE-SDSS colors.

We apply additional cuts to the WISE-SDSS matches to ensure that the SDSS detections are real objects rather than artifacts. We remove duplicate detections by only including "survey primary" detections (Stoughton et al. 2002). For matches with  $r < 22$ , we remove all detections with SDSS imaging flags indicating dirty photometry (e.g. saturated detections, cosmic ray strikes, image-processing artifacts, etc.<sup>6</sup>). We do not remove detections with  $r > 22$  and dirty photometry because these detections are faint enough to be spuriously flagged as "dirty" even if they are real objects. We also remove all detections with  $r$ -band dust extinction greater than 0.3 magnitudes.

Ignoring the WISE resolution of 6", the astrometric precision of SDSS and WISE implies that all WISE-SDSS matches should have a separation  $\lesssim 1"$ . However, since WISE has a much larger angular resolution than SDSS, we find many matches with separations between 1" and 3". Visual inspection of SDSS and WISE images shows that many matches with separations  $> 1"$  are not merely a result of imprecise WISE astrometry. Instead, two SDSS detections separated by  $< 6"$  are merged into a single WISE detection in a substantial fraction of these matches. If the second-closest SDSS detection is substantially brighter than the match, it is possible that a large portion of flux from the WISE detection should have been assigned to the second-closest SDSS detection

rather than to the match. As a result, the match may not actually meet our color cut. We remove these problematic matches by defining the SDSS match as the brightest SDSS detection within 3" of the WISE detection. This definition removes matches in which the second-closest SDSS detection is brighter than the match, leading to a spuriously high  $r - W1$  for that WISE detection. By excluding these detections, we reduce contamination in our sample.

Our final galaxy sample contains 4,168,855 objects, including 2,675,189 non-matches and 1,493,666 matches (composed of 331,327 point sources and 1,162,339 extended sources in SDSS imaging). We estimate the severity of contamination from Galactic stars by plotting the sky distribution of our sample in Galactic coordinates. We also plot the sky distribution of our sample in Ecliptic coordinates to determine whether our sample is affected by fluctuations in the WISE coverage depth due to overlapping scans<sup>7</sup> (Figure 3). We observe substantial gradients on the sky related to the Galaxy but do not observe significant gradients following the WISE scan pattern. Both the SDSS-identified extended sources and the non-matches have densities  $\sim 80\%$  greater at high Galactic latitudes. The anti-correlation with the Galactic center results from source confusion: at low Galactic latitudes, a galaxy is more likely to be masked by a Galactic star. The similarity between the sky distributions of the extended sources and the non-matches suggests that the non-matches are largely composed of  $z > 0.6$  galaxies rather than Galactic stars or spurious WISE detections.

SDSS-identified point sources display the opposite pattern, with densities nearly twice as high at low Galactic latitudes than at the poles. This indicates that a substantial fraction of the point sources are very red Galactic stars. Nevertheless, we believe it is prudent to retain the point sources in our sample. The SDSS star/galaxy separation is seeing dependent, with galaxy density decreasing in imaging with poor seeing, particularly for faint detections (Scranton et al. 2002). As a result, excluding the point sources from our sample would lead to seeing-dependent spatial variations in density, which are likely correlated with seeing-dependent spatial variations in quasar density. Given that point sources compose only 7% of our sample and that the point sources correlate significantly with the quasars (see Figure 6), we believe that is appropriate to keep the point sources in our sample to eliminate the possibility of seeing-dependent systematic error.

## 2.2. Quasar selection

In order to obtain as large a luminosity range as possible, we measure the quasar-galaxy clustering amplitude for quasars selected from two quasar catalogs, the SDSS DR7 catalog with 105,783 quasars (Shen et al. 2011) from SDSS I/II (York et al. 2000), and the DR10 catalog with 166,583 quasars (Pâris et al. 2014) from BOSS (Eisenstein et al. 2011; Dawson et al. 2013). In both SDSS I/II and BOSS, quasar candidates were selected from SDSS photometry using object colors. SDSS I/II targeted objects with  $15 < i < 19.1$  (Schneider et al. 2010),

<sup>6</sup> See [https://www.sdss3.org/dr8/algorithms/photo\\_flags\\_recommnd.php](https://www.sdss3.org/dr8/algorithms/photo_flags_recommnd.php) for definition.

<sup>7</sup> The WISE scan pattern in is given in Figure 5 in [http://wise2.ipac.caltech.edu/docs/release/allsky/expsup/sec6\\_2.html](http://wise2.ipac.caltech.edu/docs/release/allsky/expsup/sec6_2.html).

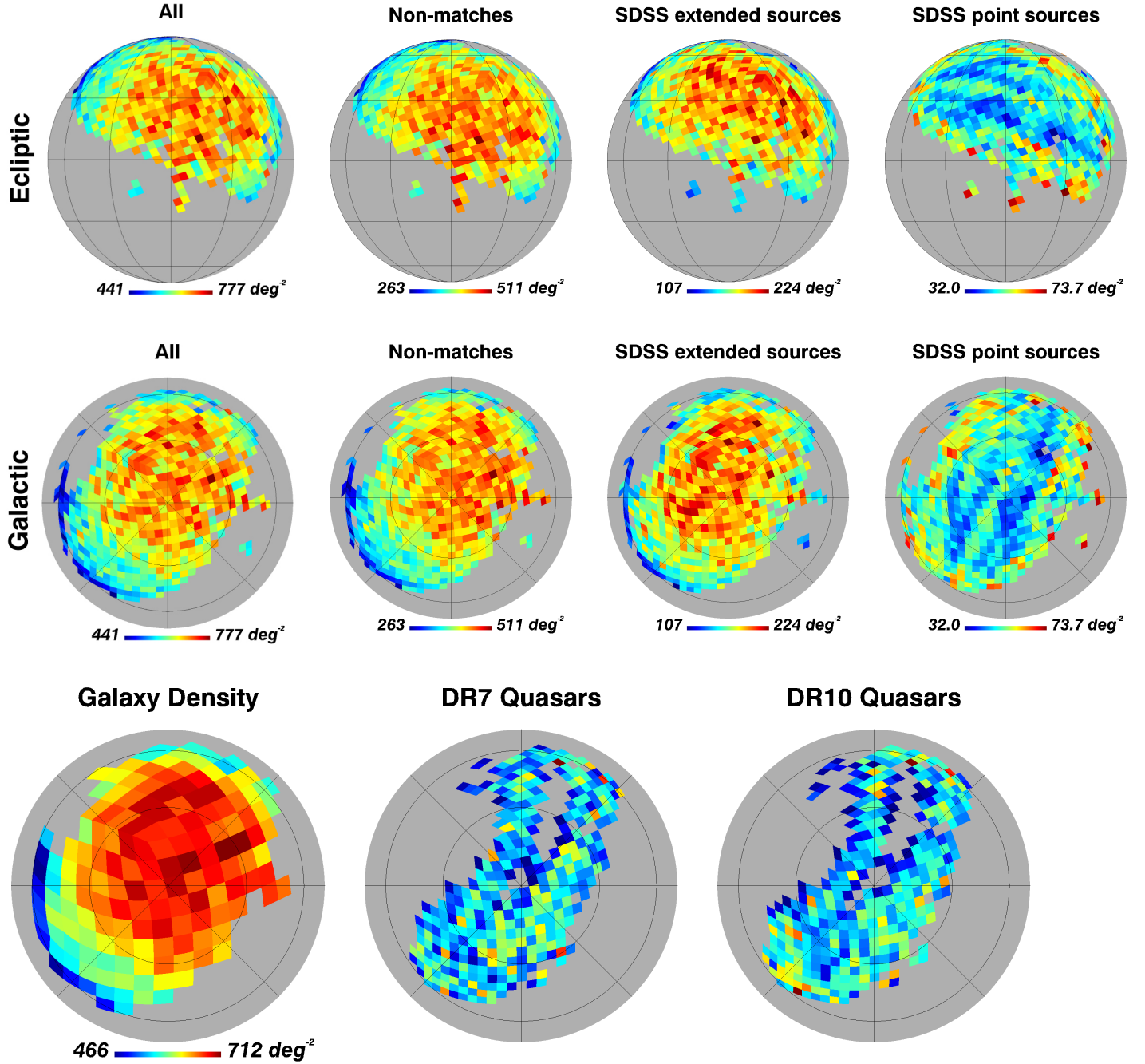


**Figure 3.** *Top and middle (left to right):* Densities of the entire galaxy sample; all WISE galaxies lacking an SDSS match; all WISE galaxies matched to an SDSS extended source; and all WISE galaxies matched to an SDSS point source. Both plots only display HEALPix pixels with more than 20% of their area covered by the Ho et al. (2012) DR8 imaging footprint. *Top:* Ecliptic coordinates with  $180^\circ$  Ecliptic longitude running through the center of the plot and longitude increasing to the left. *Middle:* Galactic coordinates with Galactic longitude increasing clockwise from the Galactic center at the bottom of each plot. While the variation in density with Galactic latitude is clearly apparent, we do not observe any variation in density in regions of deeper WISE coverage (wide strip between  $200^\circ$  and  $230^\circ$  Ecliptic longitude and  $-90^\circ$  to  $90^\circ$  Ecliptic latitude). *Bottom:* Comparison of galaxy and quasar sky distribution. *Bottom left:* galaxy density used in the calculation of the quasar-galaxy angular overdensity. Pixels with less than 20% of their area covered by the imaging footprint are excluded. *Bottom center and right:* DR7 and DR10 quasar distribution. Because of the low density of quasars, the fluctuations between pixels are dominated by shot noise rather than by intrinsic variation in quasar density. Only quasars in the region of sky covered by both DR7 and DR10 spectroscopy are displayed.

while BOSS targeted objects with either  $r < 21.85$  or  $g < 22$  (Pâris et al. 2014) and  $i > 17.8$  (Bovy et al. 2011). Quasar candidates were arranged on spectroscopic plates (Blanton et al. 2003), observed using a twin multi-object fiber-fed spectrograph (Smee et al. 2013), and reduced and classified as a quasar, galaxy or star (Bolton et al. 2012). The wavelength range is 3800 to 9200 Å for SDSS I/II and 3600 to 10400 Å for BOSS (Smee et al. 2013).

DR7 quasar candidates were selected using a uniform target algorithm based on their colors (Richards et al. 2002). The DR7 quasar catalog includes serendipitously imaged objects selected by other targeting algorithms, and we reject the half of the quasar catalog that was not selected using the uniform targeting algorithm. Quasars in DR10 are selected using a variety of methods. Half are selected uniformly to form the CORE sample, using the XDQSO method (Bovy et al. 2011), and the other half are selected inhomogeneously to maximize surface density (see Pâris et al. 2014 for details on the various selection algorithms). We only use the CORE sample in this work. Both the DR7 uniform quasars and the DR10 CORE quasars are uniformly distributed across the sky. The DR7 spectroscopic footprint is substantially larger than the DR10 footprint, because DR7 is the final data release for SDSS II while DR10 is not the final data release for SDSS III. We only use quasars that lie in the intersection of the DR7 and DR10 footprints. We also only consider quasars lying within the DR8 photometric footprint of Ho et al. (2012), since our galaxy sample is restricted to this footprint.

The final quasar sample contains 7,049 quasars with  $0.65 < z < 0.9$ , 4,206 from DR10 and 2,843 from DR7. Figure 4 shows the redshift, luminosity and virial mass distributions for the DR7 and DR10 quasars. To measure the luminosity dependence of the clustering amplitude, we split the DR7 quasars into three groups by luminosity and the DR10 quasars into four groups by luminosity. Similarly, we split the DR7 quasars into four groups by virial mass and the DR10 quasars into four groups by virial mass.

Redshifts in both the DR7 and DR10 catalogs are accurate to  $\Delta z < 0.01$  (Schneider et al. 2010, Pâris et al. 2014). In this paper, we measure luminosity using the absolute  $i$ -band magnitude  $K$ -corrected to  $z = 2$  for both DR7 and DR10 (Richards et al. 2006). These magnitudes measure the quasar luminosity in a bandpass centered at 2500 Å in the rest frame. We convert absolute magnitude to 2500 Å luminosity in  $\text{erg s}^{-1}$  using Equation 4 from Richards et al. (2006) and then to solar luminosity using  $L_{\odot} = 3.827 \times 10^{33} \text{ erg s}^{-1}$ . Reported  $i$ -band magnitude errors for quasars in our sample are  $\leq 0.03$  for DR7 and  $\leq 0.1$  for DR10. Note that the DR7 quasars are substantially more luminous than the DR10 quasars (Figure 4), since BOSS targeted fainter, higher-redshift quasars compared to SDSS I/II.

We use the single-epoch virial mass estimates from Shen et al. (2011) for DR7 quasars, and estimates computed using similar methodology for the DR10 quasars (Y. Shen, private communication)<sup>8</sup>. The virial mass esti-

mates assume that the quasar’s broad-line region (BLR) is virialized:

$$M_{\text{enc}} = M_{\text{BH}} = \frac{V_{\text{BLR}}^2 R_{\text{BLR}}}{G} \quad (2)$$

The BLR velocity is inferred from the width of a particular broad line. The radius is determined by measuring the continuum luminosity: reverberation mapping of  $z < 0.3$  AGN found a tight relationship between continuum luminosity and BLR radius (Kaspi et al. 2000). This relationship arises because the size of the BLR is regulated by the amount of ionizing radiation emitted by the quasar, which is proportional to the optical continuum luminosity. Since the reverberation mapping samples used to calibrate the single-epoch virial mass estimates use  $\text{H}\alpha$  and  $\text{H}\beta$  line widths, virial mass estimators based on  $\text{H}\alpha$  and  $\text{H}\beta$  are most reliable (Shen 2013). However,  $\text{H}\beta$  is redshifted beyond the edge of the DR7 spectrograph (9200 Å) at  $z > 0.85$ , so we instead use  $\text{MgII}$  based mass estimates.  $\text{MgII}$  line widths correlate well with  $\text{H}\beta$  line widths (Shen 2013), but the  $\text{MgII}$  masses may possess substantial systematic errors due to the lack of  $\text{MgII}$ -based reverberation mapping masses. However, since we are interested in the slope rather than the normalization of the black hole mass-clustering strength relationship, we are not concerned with systematic errors resulting in a uniform offset in black hole mass.

We are primarily concerned with two kinds of error in the virial mass estimates: increased scatter due to the large uncertainties in the virial mass estimates and a luminosity-dependent bias arising from the flux limit of the sample. First, the spread in virial mass is wider than the spread in true mass because of the large uncertainties in individual virial mass estimates. Shen (2013) estimated that the scatter in virial mass at fixed true mass is up to  $\approx 0.5$  decades, arising from both measurement errors in line width and continuum luminosity, and uncertainties in the virial mass calibrations. We reduce the measurement uncertainties slightly by excluding quasars with poor continuum or  $\text{MgII}$  emission line fits ( $\chi^2/\text{d.o.f} > 2$ ), but this does not reduce the calibration uncertainties, which are the dominant source of scatter in virial mass at fixed true mass. Because of the large uncertainty in virial mass, the dynamic range of true mass in our sample is less than the measured range in virial mass, and the mean true mass for quasars in a given virial mass bin is less extreme than the mean virial mass.

Shen (2013) also discussed a luminosity-dependent bias arising from uncertainties in line width and luminosity. Measurement errors, scatter in the radius-luminosity relationship, non-virial motion, and a time lag between changes in luminosity and radius may lead to uncorrelated errors in luminosity and line width. If uncorrelated errors are present, virial masses in flux-limited samples will be biased high relative to true masses, since the increase in average luminosity caused by the flux limit will not be entirely cancelled by a decrease in line width. The magnitude of the bias will be greatest for low luminosity subsamples that lose a substantial number of quasars to the flux limit. Shen (2013) and Shen & Kelly (2012) found evidence for luminosity-dependent bias in  $\text{MgII}$  masses. Since less massive quasars are also less lumi-

communication).

<sup>8</sup> The line fitting methodology for DR10 is described in Shen & Liu (2012) and at [http://users.obs.carnegiescience.edu/yshen/BH\\_mass/dr9.htm](http://users.obs.carnegiescience.edu/yshen/BH_mass/dr9.htm). The practical impact of the different fitting procedures for DR7 and DR10 is negligible (Y. Shen, private

nous, the luminosity-dependent bias will be stronger for low mass quasars than for high mass quasars. However, since each bin in virial mass covers a large range in true mass, the magnitude of the luminosity-dependent bias is quite similar for all virial mass bins. Because our quasar samples are flux limited, the luminosity-dependent bias causes the virial masses to systematically overestimate the true masses, but this uniform offset in black hole mass does not affect our measurement of the slope of the black hole mass-clustering strength relationship.

### 2.3. Systematic effects

The difference in redshift distribution between different quasar groups leads to systematic differences in quasar-galaxy clustering strength. The quasar luminosity function evolves significantly with redshift (Richards et al. 2006), so high luminosity quasars have a higher mean redshift than low luminosity quasars. Angular clustering strength varies with redshift due to both redshift evolution of the quasar autocorrelation function (Croom et al. 2005) and the redshift distribution of our galaxy sample. Therefore, any difference in clustering between quasar groups with different luminosities may in fact arise from the difference in redshifts.

To isolate the luminosity dependence of clustering, we assign a redshift-dependent weight to each quasar to force the weighted redshift distributions of each subsample to match the DR10 redshift distribution. For each subsample, we place the quasars into bins of width  $\Delta z = 0.01$  and compute the weights by dividing the DR10 redshift distribution by the subsample's redshift distribution. To ensure that no quasars are weighted by more than 3 or less than 1/3, we combine the two lowest-luminosity DR7 groups (see Figure 4).

Because the density of both the WISE galaxies and the stellar contaminants in the WISE sample vary across the sky, differences in large-scale sky distribution may lead to differences in clustering amplitude. Using only quasars located within the DR7/DR10 overlap region largely alleviates this problem by forcing the sky distribution of DR7 and DR10 quasars to match (see Figure 3). While the resulting sky distributions are not identical, the residual variation in both WISE galaxy density and contaminating star density is quite small. We eliminate the effects of residual variation in WISE galaxy density by measuring the galaxy density separately in each HEALPix pixel (see Górski et al. (2005) for details about HEALPix). The stellar contamination, as measured by the average fraction of SDSS point sources in the HEALPix pixel surrounding each quasar, is just 1.2% greater for DR10 quasars than for DR7 quasars. The impact of varying stellar contamination is therefore considerably lower than the magnitude of the measured overdensity  $w$ .

Small scale variations in galaxy density may also affect our clustering measurements. While Figure 3 cannot display density variations on scales less than a few degrees, we expect to observe variations in WISE density on arcminute scales due to both source suppression near bright sources and image artifacts within the halos of very bright sources<sup>9</sup>. The vast majority of these bright sources are uncorrelated with quasar positions,

so we do not apply a mask to remove the area around bright WISE sources. Unlike the large-scale variations in quasar and galaxy densities, small-scale variations in galaxy density should have the same effect on both DR7 and DR10 groups, and on different groups in luminosity and virial mass. However, bright quasars in WISE imaging may lead to both an overdensity of nearby image artifacts and an underdensity of nearby faint sources due to the increased background. While we failed to find image artifacts around the 50 brightest quasars in  $W1$ , these quasars, with  $W1 \approx 12$ , suppress the density of  $W1 = 16.5$  sources at separations  $< 18''$ <sup>10</sup>. As a result, we restrict our measurement of the quasar-galaxy cross-correlation function to angular scales  $> 18''$ , corresponding to  $\approx 0.2 h^{-1}$  Mpc. At these scales, we expect no significant suppression of galaxy density due to increased background from nearby quasars. Similar source suppression in SDSS is only observed at separations less than  $15''$  for galaxies with similar brightness as our galaxy sample about stars with similar brightness as our quasar sample (Ross et al. 2011).

## 3. MEASURING THE ANGULAR OVERDENSITY

### 3.1. Methods

In this paper, we measure the angular overdensity  $w(r_p)$  rather than the three-dimensional correlation function  $\xi(r)$  or the projected cross-correlation function  $w_p(r_p)$ . The three-dimensional quasar-galaxy cross-correlation function is well-fit by a power law (e.g. Yee & Green 1987):

$$\xi(r) = \left(\frac{r_0}{r}\right)^\gamma \quad (3)$$

where  $r_0$  is the correlation length, which is typically used to characterize clustering strength. The projected cross-correlation function  $w_p(r_p)$  is the integral of the three-dimensional cross-correlation function along the line of sight:

$$w_p(r_p) = \int_{-\infty}^{\infty} \xi(r_p, \pi) d\pi = r_0^\gamma \frac{\Gamma(1/2)\Gamma[(\gamma-1)/2]}{\Gamma(\gamma/2)} r_p^{1-\gamma} \quad (4)$$

where  $\Gamma$  is the gamma function and  $\pi$  is the line-of-sight distance. Following Zhang et al. (2013), we can relate the projected cross-correlation function  $w_p(r_p)$  to the angular overdensity  $w(r_p)$ :

$$w_p(r_p) = \left\langle \frac{n}{\rho_0} \right\rangle w(r_p) \quad (5)$$

where  $n$  is the WISE density near each quasar (Figure 3) and  $\rho_0$  is the density of galaxies at each quasar's redshift that meet our color and  $W1$  cuts.

Estimating  $r_0$  and  $b_Q$  requires finding the projected cross-correlation function, which requires an estimate of  $\rho_0$ . One can compute  $\rho_0$  by integrating the galaxy luminosity function at each redshift (e.g. Zhang et al. 2013, Komiya et al. 2013). However, this method is insufficiently precise to measure the host halo mass to a reasonable accuracy: since bias is a shallow function of host halo mass at  $z \approx 0.8$ , small errors in the luminosity function

<sup>9</sup> See [http://wise2.ipac.caltech.edu/docs/release/allsky/expsup/sec6\\_2.html](http://wise2.ipac.caltech.edu/docs/release/allsky/expsup/sec6_2.html).

<sup>10</sup> See Figure 25 at [http://wise2.ipac.caltech.edu/docs/release/allsky/expsup/sec6\\_2.html](http://wise2.ipac.caltech.edu/docs/release/allsky/expsup/sec6_2.html).

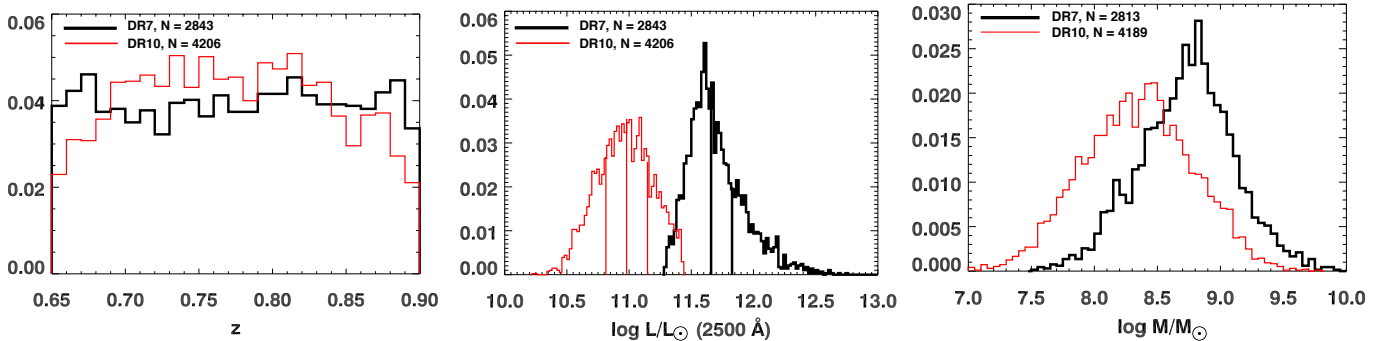


**Figure 4.** *Left:* redshift distribution for DR7 and DR10 quasars. *Center:* Distributions of  $M_i(z = 2)$  for DR7 and DR10 quasars ( $\approx 2500 \text{ \AA}$  restframe wavelength) in solar luminosities. The vertical lines divide the sample into 4 DR10 groups and 3 DR7 groups. The right-most cut in the DR10 distribution at  $11.43 \log L/L_\odot$  minimizes the overlap between the most luminous DR10 sample and the least luminous DR7 sample. *Right:* Virial black hole masses for DR7 and DR10 quasars, computed by Shen et al. (2011) from continuum luminosity and emission line widths. The DR7 and DR10 quasars are each divided into 4 groups; the divisions are not shown because several of the bins overlap.

(and thus  $\rho_0$ ,  $r_0$ , and the bias) lead to relatively large errors in the host halo mass. For instance, small differences in photometric calibration between SDSS and the instrument used to find the luminosity function will lead to substantial errors in the luminosity function, causing large uncertainties in the host halo mass. Moreover, to find  $\rho_0$  we would need to apply our color cut to the galaxy luminosity functions, requiring knowledge of galaxy SEDs at  $z \approx 0.8$ . Ultimately, finding  $r_0$  and  $b_Q$  is not necessary to measure the change in clustering with luminosity and virial mass, since such changes will be just as apparent in the angular overdensity  $w(r_p)$ . Given the difficulties associated with computing  $r_0$  and  $b_Q$  from our data, we choose to only measure the clustering dependence of  $w(r_p)$  in this paper.

We measure the angular quasar-galaxy overdensity by counting the number of excess galaxies at angular separation  $\theta$  from each quasar. We count the number of galaxies  $N$  in an annulus of width  $\Delta\theta$  and divide by the expected density of galaxies:

$$w(\theta) = \left( \sum_i w_i \frac{N_i}{n_i A_i} \right) / \left( \sum_i w_i \right) - 1 \quad (6)$$

where  $n$  is the average galaxy density,  $A$  is the area inside the SDSS imaging footprint, the index  $i$  ranges over every quasar, and the weights  $w$  are computed from the redshift distribution as described in Section 2.2. Because the galaxy density varies substantially across the sky,  $n$  is estimated by using the galaxy density in each HEALPix pixel (Figure 3). We exclude 18 quasars lying in pixels with less than 20% coverage of the imaging footprint; for these pixels, Poisson variations in the density are  $> 1\%$ , comparable in magnitude to the Galactic gradients shown in Figure 3, and thus we consider the density estimates for these quasars to be unreliable.

We determine  $A$ , the area within the imaging mask, using a Monte Carlo method. We create a catalog of random points lying outside the imaging footprint with density  $n_{\text{random}} = 2909 \text{ deg}^{-2}$ , much larger than the maximum  $n$ ,  $712 \text{ deg}^{-2}$  (Figure 3). We use this catalog to find the area within the imaging footprint,  $A$ , by subtracting the area outside the imaging footprint from the area of

the full annulus,  $A_{\text{full}}$ :

$$A = A_{\text{full}} - \frac{N_{\text{random}}}{n_{\text{random}}} \quad (7)$$

where the area outside the imaging footprint is determined by dividing the number of random points in the annulus,  $N_{\text{random}}$ , by the density of random points  $n_{\text{random}}$ . Next we transform from  $w(\theta)$  to  $w(r_p)$ , where  $r_p$ , measured in comoving  $h^{-1}$  Mpc, is the distance between the quasar and the galaxy assuming that the galaxy lies at the same redshift as the quasar. We compute the area of the full annulus,  $A_{\text{full}}$ , using  $r_p$  rather than  $\theta$ :

$$A_{\text{full}} = \pi \frac{r_2^2 - r_1^2}{((1+z)D_A)^2} \quad (8)$$

where  $r_1 = r_p - \Delta r_p$ ,  $r_2 = r_p + \Delta r_p$ , and  $D_A(z)$  is the angular-diameter distance to a quasar at redshift  $z$ .

We measure  $w(r_p)$  in the following 5 bins (in units of  $h^{-1}$  Mpc): 0.2–0.4, 0.4–0.8, 0.8–1.6, 1.6–3.2, and 3.2–6.4. We cannot measure  $w(r_p)$  at separations less than  $0.2 h^{-1}$  Mpc (angular separation  $18''$ ) because at smaller separations the density of  $W1 = 16.5$  galaxies is suppressed by the wings of the central quasar’s flux profile. At angular scales larger than  $6.4 h^{-1}$  Mpc, we find that our measurement of  $w(r_p)$  is contaminated by systematic errors (see Section 3.3).

We use bootstrap resampling to estimate our error bars. We resample by HEALPix pixel: from the 154 pixels with at least one quasar, we randomly select 154 pixels with replacement and measure  $w(r_p)$  for all quasars in the selected pixels. We use 50,000 resamples to calculate error bars and the covariance matrix. Equation 9 gives the reduced covariance matrix for the measurement of  $w$  across the entire sample,  $R_{ij} = C_{ij} / \sqrt{C_{ii} C_{jj}}$ , where  $C$  is the covariance matrix:

$$R = \begin{pmatrix} 1.000 & 0.234 & 0.230 & 0.152 & -0.005 \\ 0.234 & 1.000 & 0.336 & 0.226 & 0.025 \\ 0.230 & 0.336 & 1.000 & 0.306 & 0.220 \\ 0.152 & 0.226 & 0.306 & 1.000 & 0.595 \\ -0.005 & 0.025 & 0.220 & 0.595 & 1.000 \end{pmatrix} \quad (9)$$

Since  $w_p(r_p)$  is related by  $w(r_p)$  by a constant of pro-

portionality (Equation 5), we fit a power law to  $w(r_p)$ :

$$w(r_p) = \beta r_p^{-\delta} \quad (10)$$

where  $\beta \propto r_0^\gamma$  and  $\delta = \gamma - 1$ . We use  $\chi^2$  minimization to find the best fit values of  $\beta$  and  $\delta$  for our measurement of  $w(r_p)$  using the entire quasar and galaxy samples. Since the off-diagonal terms of the covariance matrix are nonzero (Equation 9), we compute  $\chi^2$  using the full covariance matrix. Using bootstrapping, we confirm that the sampling distribution of  $w(r)$  in each bin is very well approximated by a Gaussian, indicating that  $\chi^2$  minimization is an appropriate curvefitting technique. We will use the clustering amplitude  $\beta$  to characterize the strength of quasar-galaxy clustering for each of our subsamples.

### 3.2. Results

Figure 5 shows the measured angular overdensity and a best-fit curve, using a sample of 7,049 quasars from both DR7 and DR10. A two parameter fit yields a minimum  $\chi^2$  of 10.23 with 2 degrees of freedom,  $\beta = 0.105 \pm 0.007$ , and  $\delta = 0.84 \pm 0.05$ . Varying the minimum bin radius does not substantially affect  $\beta$  or  $\delta$ , nor does successively removing each bin from the fit.

By dividing  $w(r_p)$  by the projected correlation function of the linear-regime matter field, we obtain a quantity proportional to  $b_{\text{QG}}^2$ , the square of the linear quasar-galaxy bias (Equation 1). We plot this quantity in Figure 5. Quasar-galaxy clustering at  $0.2\text{--}6.4 h^{-1}$  Mpc arises from a mixture of one-halo and two-halo terms: the one-halo term refers to clustering within the same dark matter halo, while the two-halo term refers to clustering between different halos. One-halo clustering leads to an increase in the linear bias at  $r_p < 1 h^{-1}$  Mpc (Shen et al. 2013) and cosmological hydrodynamic simulations indicate that the one-halo term dominates clustering at  $r_p \leq 0.3 h^{-1}$  Mpc (Degraf et al. 2011). We interpret the sharp increase in linear bias at  $r_p = 0.3 h^{-1}$  Mpc (Figure 5) as evidence for one-halo clustering in this bin.

### 3.3. Testing for systematics

We check for systematic effects by measuring  $w(r_p)$  for WISE galaxies about 37,402 quasars with  $2.2 < z < 3.5$ . We randomly assign each quasar a redshift  $0.65 < z < 0.9$  so that we measure  $w(r_p)$  on the same angular scales as for our  $z \sim 0.8$  quasar sample. We expect a small signal due to the gravitational lensing of high-redshift quasars by  $z \sim 0.8$  galaxies. The galaxies magnify the high-redshift quasars, lowering the flux limit in the region near the galaxy and creating a cross-correlation (Myers et al. 2003, 2005, Scranton et al. 2005, Ménard et al. 2010). The strength of this signal is proportional to the magnification  $\mu$ :

$$w(r_p) \propto \mu \approx \frac{\theta_E}{\theta} \quad (11)$$

where  $\theta_E$  is the Einstein radius for a galaxy in our sample (typically  $\approx 1''$  for galaxies at  $z \approx 0.8$ ) and  $\theta$  is the angular separation between the galaxy and the quasar. The strength of this signal depends on both the level of contamination by low-redshift galaxies and stars and the average apparent magnitude of the quasar population. A linear least squares fit of constant  $r_p w(r_p)$  yields

$r_p w(r_p) = -0.0018 \pm 0.0023$ . However, for bins centered at  $1000''$  and  $2000''$  ( $9.6$  and  $19.2 h^{-1}$  Mpc at  $z = 0.8$ , respectively), we find a  $2\text{--}3 \sigma$  deviation from zero, with  $w(r_p) \approx 0.003$  for these two bins. Since the gravitational lensing signal peaks at much smaller angular scales, we attribute this large-scale overdensity to a systematic error present on all scales. While this error is very small compared to  $w(r_p)$  at smaller scales, it is close enough to  $w(r_p)$  for the bins at  $r_p = 9.6$  and  $19.2 h^{-1}$  Mpc that we restrict our measurement of angular clustering to separations of  $0.2\text{--}6.4 h^{-1}$  Mpc.

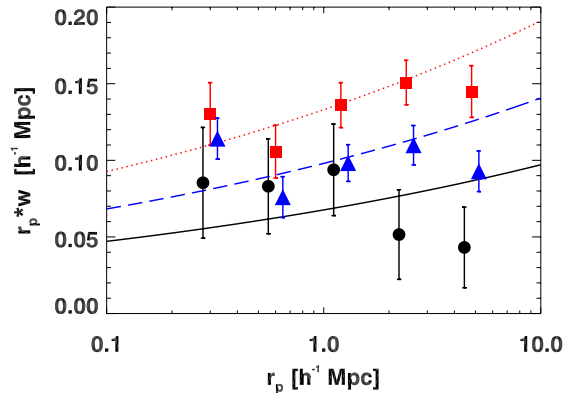


**Figure 6.** Correlations between the DR7 and DR10 quasars and SDSS-identified extended sources (red squares, dotted line), non-matches (blue triangles, long-dashed line), and point sources (black circles, solid line). The lines are linear least squares curvefits using  $\delta = 0.84$ , the slope from the two parameter fit in Figure 5. Angular clustering amplitudes at  $1 h^{-1}$  Mpc: extended sources,  $\beta = 0.134 \pm 0.009$ ; non-matches,  $\beta = 0.098 \pm 0.008$ ; point sources,  $\beta = 0.068 \pm 0.014$ .

We separately cross-correlate each of the three components of the sample (SDSS-identified point sources, extended sources, and non-matches) with the full quasar sample and measure a clustering amplitude at  $1 h^{-1}$  Mpc at least  $5 \sigma$  greater than zero for all three cases (Figure 6). The clustering amplitude for the SDSS point sources and the non-matches are 3 and 4  $\sigma$  lower than the clustering amplitudes for the SDSS extended sources, respectively, indicating that the non-matches and point sources contain more contaminating stars and low redshift galaxies than the extended sources. Nevertheless, all three components contain  $0.65 < z < 0.9$  galaxies, and we believe it is prudent to include all three components in our sample to eliminate the possibility of seeing-dependent variations in galaxy density.

## 4. DEPENDENCE OF CLUSTERING AMPLITUDE ON QUASAR PROPERTIES

We measure  $w(r_p)$  for seven groups spanning 1.3 decades in luminosity and eight groups spanning 1.3 decades in virial mass. The seven groups in luminosity consist of three DR7 groups and four DR10 groups, while the eight groups in virial mass consist of four DR7 groups and four DR10 groups (see Figure 4 for luminosity and virial black hole mass distributions).

We use linear least squares to find the clustering amplitude at  $1 h^{-1}$  Mpc ( $\beta$ ) and its standard deviation for each group, using all five radial bins in each fit. Since we

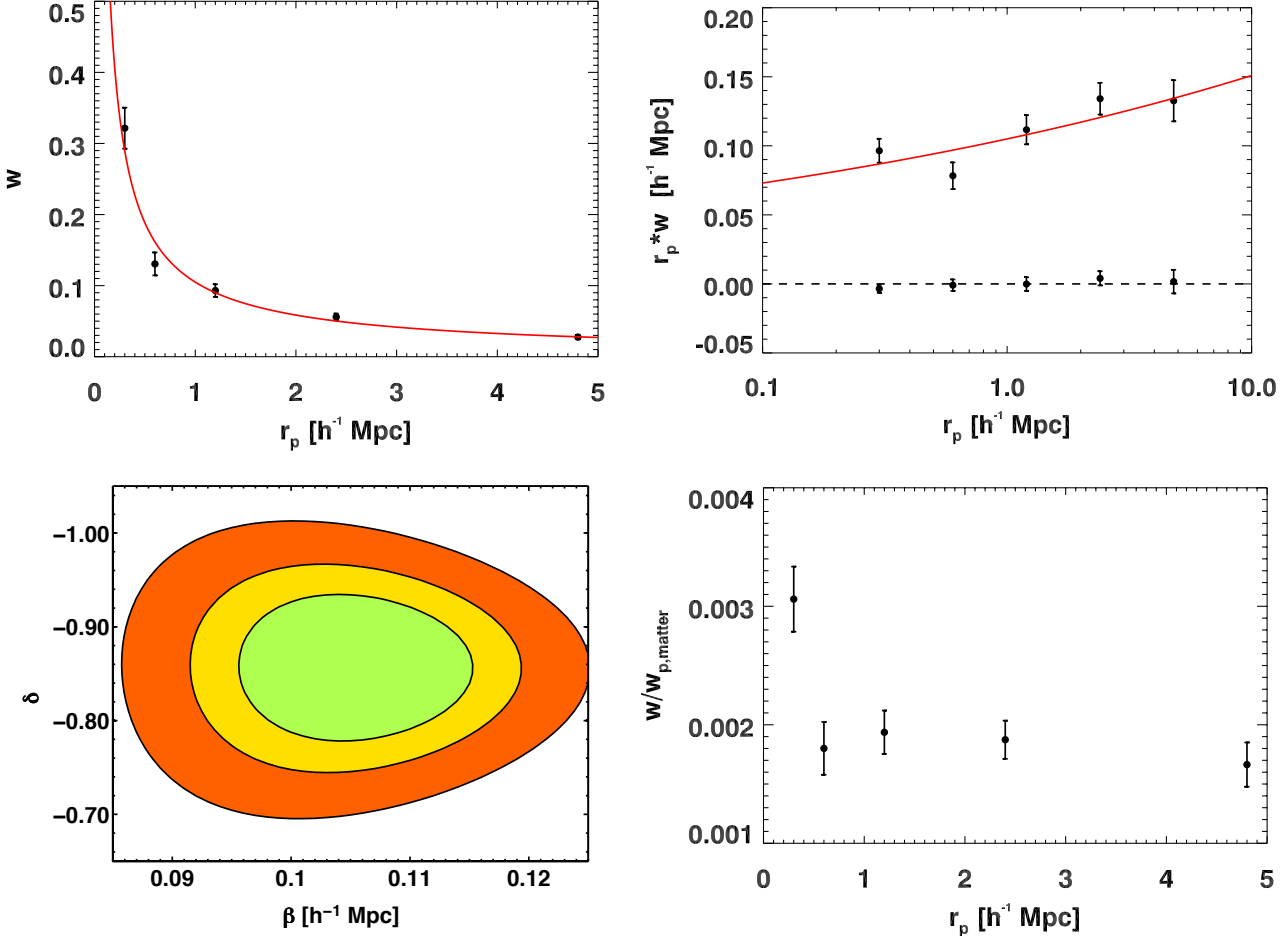


**Figure 5.** *Top left:* Angular overdensity  $w(r_p)$  and two-parameter curvefit  $w = \beta r_p^{-\delta}$  for the cross-correlation of 4.2 million WISE galaxies about 7,049 quasars from DR7 and DR10. Errorbars are  $1 \sigma$ , and  $r_p$  is measured in comoving  $h^{-1}$  Mpc. *Top right:* Same data as the top left panel, but with the  $y$ -axis replaced by  $r_p w(r_p)$  to show that we measure a significant overdensity of galaxies even at separations  $> 1 h^{-1}$  Mpc. The curvefit is shown in red. The lower points are from the cross-correlation of the WISE galaxies with 37,402  $2.2 < z < 3.5$  quasars, measured in the same angular bins as the  $z \sim 0.8$  sample. *Bottom left:*  $\chi^2$  contour for  $\delta$  and  $\beta$  with 68%, 90%, and 99% confidence intervals. *Bottom right:*  $w(r_p)$  divided by the projected correlation function of the linear-regime matter field,  $w_{p,\text{matter}}(r_p)$ , yielding a quantity proportional to the quasar-galaxy bias  $b_{\text{QG}}^2$ .

do not expect the power-law slope to vary with luminosity or black hole mass, we fix the slope at  $\delta = 0.84$  in each fit. If we allow the slope to vary, our results for  $\beta$  differ by less than  $0.3 \sigma$  for all luminosity and black hole mass subsamples. Table 1 gives the luminosity, virial mass, clustering amplitude and  $\chi^2$  for each of these samples, Figure 7 plots luminosity against clustering amplitude for the seven groups in luminosity and virial mass against clustering amplitude for the eight groups in virial mass.

We do not observe any luminosity dependence in the quasar-galaxy clustering amplitude. We fit a power law between luminosity  $L$  and clustering amplitude  $\beta$ :

$$\beta = a \left( \frac{L}{10^{11.32}} \right)^p \quad (12)$$

The factor in the denominator,  $10^{11.32}$ , is the geometric mean of the luminosities for each of the seven bins. We find  $p = d \log \beta / d \log L = -0.01 \pm 0.06$ ,  $a = 0.105 \pm 0.006$  and  $\chi^2 = 4.75$  with 4 degrees of freedom.

We also find no relationship between quasar-galaxy clustering amplitude and virial black hole mass (Fig-

ure 7). We fit a power law between virial mass  $M$  and clustering amplitude  $\beta$ :

$$\beta = a \left( \frac{M}{10^{8.54}} \right)^p \quad (13)$$

As before, the factor in the denominator is the geometric mean of the virial masses of the eight bins. Minimizing  $\chi^2$  yields  $p = 0.02 \pm 0.06$ ,  $a = 0.106 \pm 0.006$  and  $\chi^2 = 3.88$  with 5 degrees of freedom.

Since the continuum luminosity is used to estimate virial black hole mass (Equation 2),  $i$ -band luminosity and virial black hole mass are correlated (correlation coefficient  $\rho = 0.40$ ), and the constraints on luminosity dependent clustering and black hole mass dependent clustering are not independent. In order to provide an independent constraint on clustering, we also measure the dependence of clustering on MgII FWHM. If the luminosity (and therefore the broad-line region radius) is held constant, all of the variation in line width can be attributed to variation in black hole mass. We find that dividing the DR7 quasars into four equally sized groups based on MgII

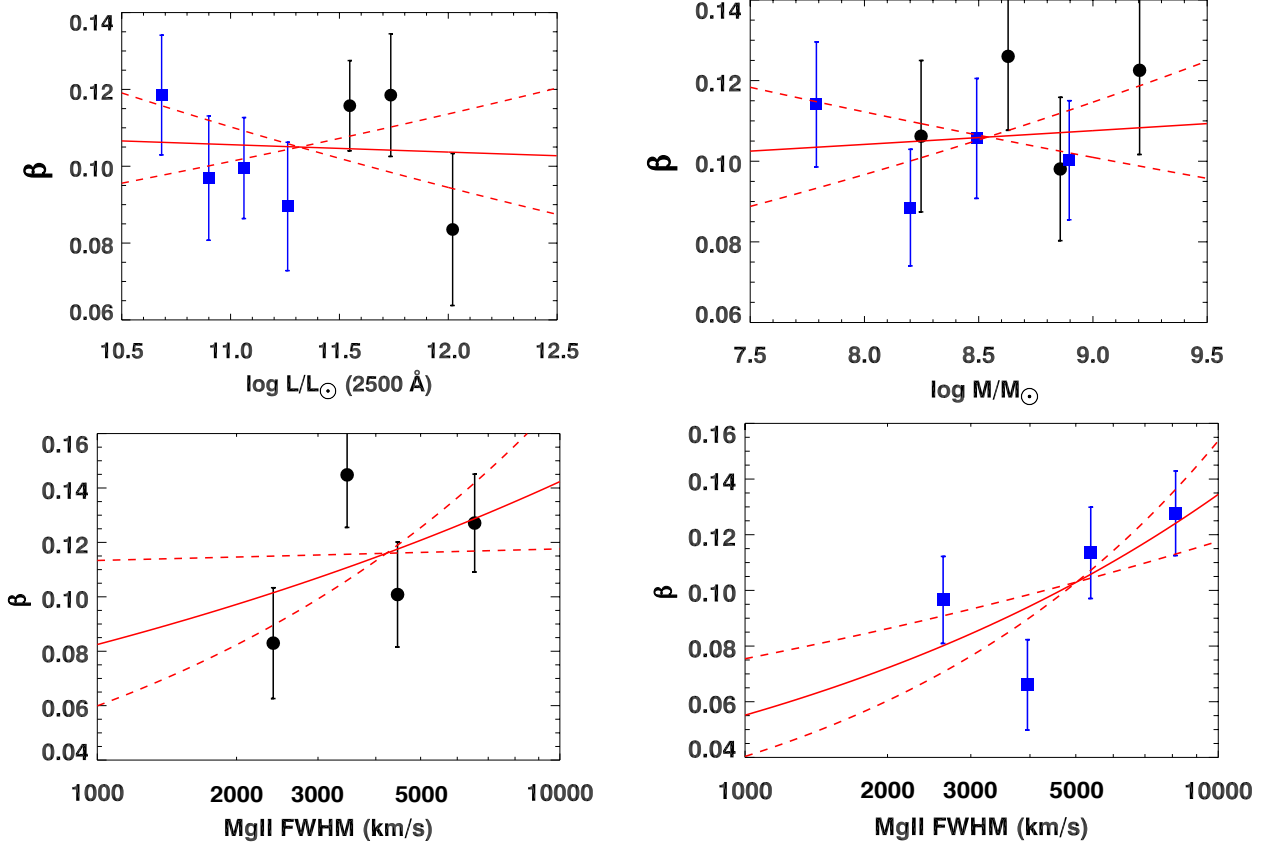


**Figure 7.** Luminosity dependence (*top left*), virial black hole mass dependence (*top right*), and MgII FWHM dependence (*bottom*) of  $\beta$ , the clustering amplitude at  $1 h^{-1}$  Mpc. Luminosity dependence and virial mass dependence are presented for both DR7 (black circles) and DR10 (blue squares) together, and FWHM dependence is presented separately for DR7 (*bottom left*) and DR10 (*bottom right*).  $\beta$  is determined from a linear least squares power-law fit to  $w(r_p)$  measured in the five radial bins of Figure 5 with  $\delta$  fixed at 0.84. Error bars are  $1 \sigma$ . The best-fit power law is shown in red. The red dashed lines are power laws with the same amplitude as the best-fit power law, but slopes  $\pm 1\sigma$  from the best fits.

**Table 1**

Quasar Sample	Galaxy Sample	$N_{QSO}$	$\log L/L_{\odot}$	$\log M_{BH}/M_{\odot}$	$\beta \pm 1\sigma$	$\chi^2$
DR7 and DR10, $0.65 < z < 0.9$	All	7049	11.28	8.49	$0.105 \pm 0.006$	10.23
DR7 and DR10, $0.65 < z < 0.9$	Point sources	7049	11.28	8.49	$0.068 \pm 0.014$	2.45
DR7 and DR10, $0.65 < z < 0.9$	Extended sources	7049	11.28	8.49	$0.133 \pm 0.009$	4.72
DR7 and DR10, $0.65 < z < 0.9$	Non-matches	7049	11.28	8.49	$0.098 \pm 0.008$	8.63
DR10, $0.65 < z < 0.9$ , $\log L < 10.81 \log L_{\odot}$	All	1052	10.68	8.10	$0.119 \pm 0.016$	6.11
DR10, $0.65 < z < 0.9$ , $10.81 \log L_{\odot} < \log L < 10.98 \log L_{\odot}$	All	1051	10.90	8.29	$0.097 \pm 0.016$	14.76
DR10, $0.65 < z < 0.9$ , $10.98 \log L_{\odot} < \log L < 11.15 \log L_{\odot}$	All	1052	11.06	8.41	$0.100 \pm 0.013$	1.33
DR10, $0.65 < z < 0.9$ , $11.15 \log L_{\odot} < \log L < 11.43 \log L_{\odot}$	All	865	11.26	8.54	$0.090 \pm 0.017$	4.49
DR7, $0.65 < z < 0.9$ , $\log L < 11.66 \log L_{\odot}$	All	1422	11.55	8.64	$0.116 \pm 0.012$	1.16
DR7, $0.65 < z < 0.9$ , $11.66 \log L_{\odot} < \log L < 11.83 \log L_{\odot}$	All	711	11.74	8.71	$0.119 \pm 0.016$	5.90
DR7, $0.65 < z < 0.9$ , $\log L > 11.83 \log L_{\odot}$	All	710	12.02	8.92	$0.084 \pm 0.020$	5.72
DR10, $0.65 < z < 0.9$ , $\log M_{BH} < 8.04 \log M_{\odot}$	All	1047	10.88	7.79	$0.114 \pm 0.016$	3.92
DR10, $0.65 < z < 0.9$ , $8.04 \log M_{\odot} < \log M_{BH} < 8.35 \log M_{\odot}$	All	1047	10.96	8.20	$0.088 \pm 0.014$	3.87
DR10, $0.65 < z < 0.9$ , $8.35 \log M_{\odot} < \log M_{BH} < 8.64 \log M_{\odot}$	All	1047	11.01	8.49	$0.106 \pm 0.015$	2.21
DR10, $0.65 < z < 0.9$ , $\log M_{BH} > 8.64 \log M_{\odot}$	All	1048	11.11	8.90	$0.100 \pm 0.015$	2.00
DR7, $0.65 < z < 0.9$ , $\log M_{BH} < 8.51 \log M_{\odot}$	All	703	11.62	8.25	$0.106 \pm 0.019$	4.05
DR7, $0.65 < z < 0.9$ , $8.51 \log M_{\odot} < \log M_{BH} < 8.76 \log M_{\odot}$	All	703	11.68	8.63	$0.126 \pm 0.018$	2.12
DR7, $0.65 < z < 0.9$ , $8.76 \log M_{\odot} < \log M_{BH} < 8.99 \log M_{\odot}$	All	703	11.71	8.86	$0.098 \pm 0.018$	1.42
DR7, $0.65 < z < 0.9$ , $\log M_{BH} > 8.99 \log M_{\odot}$	All	704	11.80	9.20	$0.123 \pm 0.020$	8.74

**Note.** — Clustering amplitude ( $\beta$ ), standard deviation,  $\chi^2$ , sample size, and mean luminosity and virial black hole mass for the quasar subsamples. The mean luminosity and virial mass are weighted using the DR10 redshift distribution ( $\bar{z} = 0.77$ ) divided by the redshift distribution of each quasar subsample. The clustering amplitudes are derived from the measurements of  $w(r_p)$  using two-parameter  $\chi^2$  minimization for the fit to the combined data (first row) and linear least squares assuming  $\delta = 0.84$  for all other subsamples.

FWHM produces four groups with very similar luminosity distributions; similarly, dividing the DR10 quasars into four equally sized MgII FWHM groups produces four very similar luminosity distributions. Since the DR7 and DR10 quasars have very different luminosity distributions, we compute the MgII FWHM dependence of clustering separately for DR7 and DR10. We also remove quasars with MgII rest-frame equivalent width  $< 10 \text{ \AA}$  from our sample (6 in DR7 and 13 in DR10) because Shen et al. (2011) find that if the equivalent width is low, the FWHM of low S/N quasars is biased low (see their Figure 7). For DR7, we find  $p = 0.24 \pm 0.22$ , and for DR10, we find  $p = 0.39 \pm 0.19$  for a power-law fit between clustering amplitude and MgII FWHM. While these results hint at a FWHM-dependent trend, more data is needed to determine whether clustering is better correlated with FWHM than with virial mass.

Simulations indicate that the luminosity and black-hole mass dependence of clustering is stronger for the one-halo term than for the two-halo term (Kauffmann & Haehnelt 2002, Thacker et al. 2009). Since we interpret the sharp increase in bias at  $r_p = 0.3 h^{-1} \text{ Mpc}$  (Figure 5) as indicative of one-halo clustering in this bin, we measure the luminosity and black hole mass dependence of clustering using this bin only to isolate the luminosity and black hole mass dependence of one-halo clustering. We do not detect luminosity or virial mass dependence of clustering in the smallest bin: for the luminosity dependence we find  $p = 0.03 \pm 0.11$ ,  $a = 0.33 \pm 0.03$  and  $\chi^2 = 7.16$  with 4 degrees of freedom, whereas for the virial mass dependence we find  $p = 0.14 \pm 0.11$ ,  $a = 0.32 \pm 0.03$  and  $\chi^2 = 8.54$  with 5 degrees of freedom.

To verify the robustness of our results, we repeat the measurements of luminosity and virial mass dependent clustering using different samples of quasars and galaxies. We restrict the galaxy sample first by excluding SDSS-identified point sources and then by also excluding non-matches. When we exclude point sources, we find identical slopes in the  $\beta$ -luminosity and  $\beta$ -virial mass relationships. When we exclude both point sources and non-matches, we find that the slopes of the  $\beta$ -luminosity and  $\beta$ -virial mass relations are lower by about  $2\sigma$ . This suggests that our results are not affected by systematic errors arising from the sample composition.

We also study the black hole mass dependence of clustering using virial masses from H $\beta$  instead MgII. We use a restricted redshift range,  $0.65 < z < 0.85$ , to ensure that the entire H $\beta$  profile is measured by the DR7 spectrograph. We obtain a slope of  $p = 0.07 \pm 0.07$  for the H $\beta$  masses compared to  $p = 0.00 \pm 0.06$  for the MgII masses in this range. Thus, we detect no dependence of clustering amplitude on either H $\beta$  or MgII based virial masses.

As discussed in Section 2.2, the virial black hole masses possess significant uncertainties of up to 0.5 decades (Shen 2013). As a result, the mean true mass of each bin is less extreme than the mean virial mass, suppressing the virial mass dependence of quasar-galaxy clustering. We estimate this suppression by simulating our data using an assumed power-law relationship between  $\beta$  and true mass, scattering true mass to virial mass, binning the simulated data by virial mass, and fitting a power

law to the binned data. We then find the ratio between the assumed power law slope and the fitted slope. To find the distribution of true black hole masses, we approximate our observed virial mass distribution as lognormal with scatter  $\sigma_{\text{obs}}$  (0.38 decades for DR7 and 0.43 decades for DR10) and assume that the distribution of virial masses at fixed true mass is lognormal with scatter  $\sigma_{\text{vir}}$ ; then the true mass distribution is lognormal with scatter  $\sigma_{\text{true}} = \sqrt{\sigma_{\text{obs}}^2 - \sigma_{\text{vir}}^2}$ . Previous measurements of the black hole mass function, using virial masses but explicitly modelling both the luminosity-dependent bias and the Malmquist bias, found  $\sigma_{\text{true}} = 0.26$  and  $\sigma_{\text{vir}} = 0.26$  for DR7 quasars at  $z = 0.8$  (Shen & Kelly 2012).

We compute the ratio between the assumed power-law slope and the measured power-law slope for different values of  $\sigma_{\text{vir}}$ , finding that the ratio reaches 2 at  $\sigma_{\text{vir}} = 0.33$  ( $\sigma_{\text{true}} = 0.19$  for DR7, 0.28 for DR10) and asymptotes as  $\sigma_{\text{vir}}$  approaches  $\sigma_{\text{obs}}$ . We also note that if luminosity-dependent bias is present,  $\sigma_{\text{true}} > \sqrt{\sigma_{\text{obs}}^2 - \sigma_{\text{vir}}^2}$ , since the luminosity-dependent bias will decrease the observed scatter in the virial masses. Since Shen (2013) and Shen & Kelly (2012) find evidence for luminosity-dependent bias for MgII-based masses at  $z = 0.8$ ,  $\sigma_{\text{vir}} = 0.3 - 0.35$  is most consistent with previous measurements of the black hole mass function and estimates of  $\sigma_{\text{vir}}$ . This value of  $\sigma_{\text{vir}}$  corresponds to a suppression of the power-law slope by a factor of 1.5–2.

## 5. DISCUSSION

### 5.1. Slope of the correlation function

Comparing the clustering amplitude  $\beta$  to previous measurements of the correlation length  $r_0$  is beyond the scope of this paper, since it would require converting our measurements of the angular overdensity to measurements of the projected cross-correlation function using the three-dimensional density of WISE galaxies  $\rho_0$  (Equation 5). However, because of the scale independence of the power law fit, we can compare our power-law slope,  $\delta = 0.84 \pm 0.05$ , to other results, using Equation 4 to relate  $\delta$  to other measurements of  $\gamma = \delta + 1$ . Coil et al. (2007) finds  $\gamma$  between 1.6 and 2 depending on the sample, with  $1\sigma$  errorbars  $\sim 0.2$ . Porciani & Norberg (2006) find  $\gamma = 1.7^{+0.53}_{-0.67}$  for quasars and galaxies with redshift  $0.8 < z < 1.06$ , Shen et al. (2013) finds  $\gamma = 1.69 \pm 0.07$  for redshifts  $0.3 < z < 0.9$ , and Zhang et al. (2013) finds  $\gamma = 2.1 \pm \sim 0.2$  for redshifts  $0.6 < z < 1.2$ .

Our measurement of  $\delta$  is similar to most of these results, although very slightly higher. A slightly steeper correlation function is to be expected for our sample: our color cut biases the galaxy sample in favor of red galaxies, which cluster more strongly than blue galaxies. According to the galaxy autocorrelation function measurements of Zehavi et al. (2011), red galaxies have  $\gamma = 1.94 \pm 0.03$ , whereas blue galaxies have  $\gamma = 1.66 \pm 0.03$ . Furthermore, we may measure a steeper slope because we measure quasar-galaxy clustering at smaller scales than previous studies. While we measure clustering from  $0.2 - 6.4 h^{-1} \text{ Mpc}$ , Coil et al. (2007) measure clustering from  $0.1 - 10 h^{-1} \text{ Mpc}$ , Porciani & Norberg (2006) measure clustering from  $3 - 20 h^{-1} \text{ Mpc}$ , and Shen et al. (2013) measure clustering from  $2 - 25 h^{-1} \text{ Mpc}$ . Therefore, our measurements are more sensitive to the one-halo term than previous

measurements, leading to a steeper power law slope at scales  $< 1 h^{-1}$  Mpc (e.g. Shen et al. 2013). Indeed, our results suggest a break in the power law at  $1 h^{-1}$  Mpc, with a steeper slope at smaller scales and a shallower slope at larger scales (see Figure 5). However, we do not have enough bins to fit either a full halo occupation distribution (HOD) function or a broken power law.

### 5.2. Luminosity dependent clustering: comparison to previous results

We find no dependence of clustering amplitude upon luminosity (Figure 7). We measure the luminosity dependence of clustering across a larger luminosity range and with more bins in luminosity than previous studies at similar redshifts. As a result, our power-law fit of clustering amplitude versus luminosity provides a similar or tighter constraint on the luminosity dependence of quasar clustering than previous results.

Most previous studies of luminosity dependent clustering measure the correlation length  $r_0$  as a function of luminosity. Since  $r_0 \propto \beta^{1/\gamma} = \beta^{0.55}$  (Equation 4), we fit a power law between luminosity and  $\beta^{0.55}$  to compare our results to previous results, using errors computed from Taylor series error propagation. We find a slope of  $0.002 \pm 0.027$ . A power law is advantageous because it is scale independent, allowing us to compare our slope to the slopes obtained from power-law fits between  $r_0$  and luminosity. When fitting power laws to other results, we assume uncorrelated errors and use the same non-linear  $\chi^2$  minimization used to determine the amplitude and slope of the power law fit to our data. We compare to measurements of  $r_0$  rather than to measurements of the quasar bias  $b_Q$  because measurements of the quasar bias incorporate errors arising from measurement of the galaxy bias.

Zhang et al. (2013), measuring the cross-correlation of SDSS Stripe 82 galaxies and SDSS quasars at  $z \sim 0.8$ , found no significant differences in clustering between two bins in luminosity with 10–25% error on the clustering measurements. Zhang et al. (2013) compared the clustering of faint and bright quasars for three different redshift bins, yielding six bins in luminosity but with differing redshift distributions. In order to fit a power law to the correlation length measurements of Zhang et al. (2013), we normalize their correlation length measurements in the  $0.8 < z < 1.0$  and  $1.0 < z < 1.2$  bins so that the average correlation length in each redshift bin is identical. We obtain a power law slope of  $-0.01 \pm 0.10$  for the Zhang et al. (2013) measurements, for quasars at  $\bar{z} = 0.9$  and  $10.98 < \log L_\odot < 11.57$ .

Shanks et al. (2011) compared correlation lengths measured by SDSS, 2QZ, and 2SLAQ at  $z = 1.4$  across slightly more than a decade in luminosity ( $11.44 < \log L_\odot < 12.48$ ). A power law fit to their results yields a slope of  $0.04 \pm 0.03$ , providing a similar constraint on the magnitude of luminosity-dependent clustering as our result, although the measurements of Shanks et al. (2011) are at higher redshift than our results.

Shen et al. (2013), measuring the cross-correlation of DR10 CMASS galaxies and DR7 quasars at  $0.3 < z < 0.9$  ( $\bar{z} = 0.53$ ) with  $11.19 < \log L_\odot < 11.88$ , found no luminosity dependence over four bins in luminosity. We fit a power law to the Shen et al. (2013) measurements of lu-

minosity and correlation length, obtaining an exponent  $p = -0.01 \pm 0.05$ . While the clustering measurements in each bin of Shen et al. (2013) have  $\approx 10\%$  errors in  $\xi(r)$ , compared to our errors of  $\approx 15\%$  in  $w(r_p)$ , we provide a tighter constraint on the luminosity dependence of clustering because we measure clustering across a larger luminosity range and with more bins in luminosity.

Comparison of our work to previous work shows that measuring clustering across a wide range of luminosity is important in obtaining a more precise measurement of (or constraint on) luminosity-dependent clustering. The restricted range in optical luminosities is often cited as a justification for the lack of measured luminosity dependence (e.g. Bonoli et al. 2009) and the wider luminosity range probed by X-ray selected AGN may explain why X-ray luminosity dependent clustering has been detected while optical luminosity dependent clustering has not (Krumpe et al. 2012).

### 5.3. Luminosity dependent clustering: comparison to models

In Figure 8, we compare our results to theoretical predictions of luminosity-dependent clustering from four different models of quasar evolution: Shen (2009), referred to as S09, Hopkins et al. (2014) (H14), Conroy & White (2013) (CW13), and a simple “lightbulb” model used by Hopkins et al. (2007) for comparison to more sophisticated models. The S09 and H14 models are physically motivated, while the CW13 and lightbulb models merely provide a relationship between halo mass and quasar luminosity.

The “lightbulb” model is the simplest of the four considered. We use the relationship given at  $z = 1$  in Figure 3 in Hopkins et al. (2007) (the line labelled “All QSO at  $L = L_{\text{Edd}}$ ”). In this model, all quasars radiate at the same Eddington ratio and black hole mass is related to host halo mass without scatter. Thus, the luminosity-bias relationship is entirely determined by the halo mass-bias relationship. However, observation of scatter in both the Eddington ratio distribution (Shen et al. 2008, Kollmeier et al. 2006) and in the halo mass-black hole mass relationship (Ferrarese 2002) indicate that the lightbulb model is an oversimplification. The CW13 model (using the  $z = 1$  relationship from Figure 8) is a “scattered lightbulb” model with scatter in both the Eddington ratio distribution and in the black hole mass-host halo mass relation. Similar to the lightbulb model, the CW13 model uses a step function for the quasar light curve and uses the quasar lifetime to set the quasar bias at a given redshift.

In contrast, both the S09 and H14 models are based on physically motivated light curves. The H14 model (using the  $z = 1.5$  bias-luminosity relationship in their Figure 5) considers two modes of quasar fueling: major merger induced fueling, which is responsible for most high luminosity quasars, and stochastic fueling mechanisms such as minor mergers, which are responsible for lower luminosity quasars. The merger-induced fueling model is quite similar to Hopkins et al. (2007), and predicts from merger simulations that host halo mass and peak quasar luminosity are tightly linked (Lidz et al. 2006). However, the relationship between peak luminosity and instantaneous luminosity has considerable scatter, arising from the merger-based quasar light curve of Hopkins et al.

(2005). H14 also considers stochastic accretion from low-luminosity quasars and Seyfert galaxies, which reside in disk hosts rather than bulges, although the fraction of disk-hosted quasars at the luminosities of our sample is estimated to be quite small. In the H14 model, quasars spend most of their lives accreting at low rates. As a result, many faint quasars have high peak luminosities and thus high host halo masses. Thus, a large range in instantaneous luminosity maps to a small range in peak luminosity (and thus black hole mass, halo mass, and clustering strength).

The S09 model (using the relationship at  $z = 1$  from their Figure 5) is similar to H14, differing in only three respects. First, S09 estimates the major merger rate using simulations while H14 estimates the merger rate from empirical halo distribution models. Second, H14 derive their quasar light curve from simulations of galaxy mergers, while S09 fits the light curve empirically from observations. Last, S09 does not consider alternative fueling mechanisms for low-luminosity quasars, but, as discussed in the paragraph above, the practical significance of this choice is small.

Each model specifies the relationship between the linear quasar bias  $b_Q$  and the quasar luminosity. In analogy with Equation 1, the linear bias  $b_Q$  is defined using the quasar-galaxy cross-correlation function:

$$b_Q = \frac{\xi_{QG}}{b_G \xi_{\text{matter}}} \quad (14)$$

If a linear quasar bias provides an appropriate fit to our data, then Equations 3, 4, and 5 imply that  $\beta \propto b_Q$ . To compare our results to models predicting the luminosity dependence of quasar bias, we convert  $b_Q$  to  $w(r_p)$  by forcing each model to match the median  $\beta$  at the median luminosity of our data.

The linear quasar bias is only applicable on larger scales. At scales  $< 1 h^{-1}$  Mpc, the one-halo term leads to nonlinear clustering and deviations from Equation 14, as shown in Figure 5. However, Figure 5 implies that a linear bias is appropriate in all bins except the innermost bin, implying that  $\beta \propto b_Q$  is not an unreasonable assumption. Moreover, we expect that one-halo clustering will also depend on luminosity, perhaps more strongly than two-halo clustering (Kauffmann & Haehnelt 2002, Thacker et al. 2009).

The models present luminosity in different units. The S09 model gives the relationship between bias and bolometric luminosity in  $\text{erg s}^{-1}$ . We convert to  $M_i(z = 2)$  using Equation 1 from Shen et al. (2009) and then to solar luminosity using the same methods as in this paper. The H14 and lightbulb models express luminosity in terms of solar bolometric luminosity; we convert to  $\text{erg s}^{-1}$  using the bolometric luminosity of the sun,  $L_\odot = 3.827 \times 10^{33} \text{ erg s}^{-1}$ . As before, we then use Equation 1 from Shen et al. (2009) to convert to  $M_i(z = 2)$  and the same relationship used in this paper to convert to solar luminosity. The CW13 model gives luminosity using  $M_i(z = 2)$ , which we again convert to solar luminosity following the methods used above.

The H14 model provides the best fit to our data ( $\chi^2 = 5.96$  for 6 degrees of freedom), followed by the S09 model ( $\chi^2 = 6.43$ ), the CW13 model ( $\chi^2 = 10.38$ ), and the lightbulb model ( $\chi^2 = 11.22$ ) (Figure 8). Our data prefer

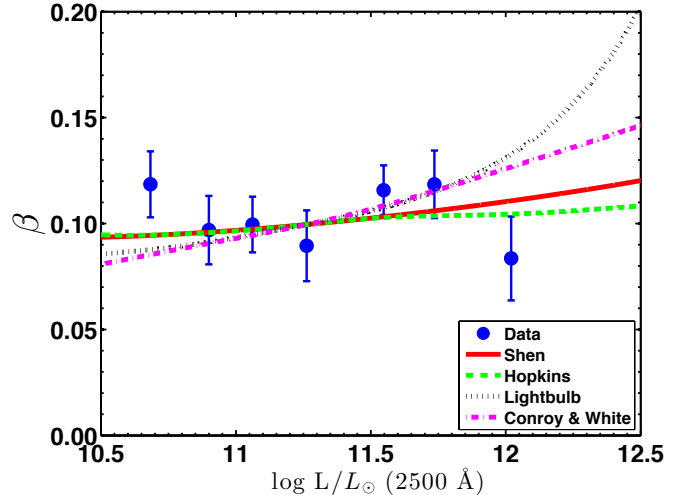


**Figure 8.** Measured clustering amplitude as a function of luminosity, compared to theoretical predictions. All four theoretical models predicted quasar bias as a function of luminosity. We assumed that quasar bias is proportional to clustering amplitude and normalized the relationship to the correlation amplitude of the median luminosity bin. Luminosities are measured using  $M_i(z = 2)$ , measured in solar luminosities, corresponding to rest-frame 2500 Å luminosity.

the H14 model to the lightbulb model at  $2 \sigma$ . However, at present none of these models are disfavored by our data at more than  $2 \sigma$ . The divergence between models is greatest at high luminosities, suggesting that improved constraints could be obtained by measuring clustering at higher redshifts, or by using a deeper sample of tracer objects to obtain more precise clustering measurements.

#### 5.4. Black hole mass dependent clustering

We find no significant relationship between virial black hole mass and clustering strength, in contrast to previous measurements of black hole mass dependent clustering by Fine et al. (2006) and Komiya et al. (2013). Our methods are quite different from the methods of Fine et al. (2006); they measured the relationship between black hole mass and host halo mass for bins at different redshift, allowing them to probe a larger dynamic range in black hole mass. Moreover, Fine et al. (2006) measured only a weak relationship between black hole mass and host halo mass. Our results are in more significant tension with those of Komiya et al. (2013): a power-law fit to the black hole mass dependence of the correlation length  $r_0$  from the data of Komiya et al. (2013) yields a slope of  $0.14 \pm 0.05$ , compared to a slope of  $0.01 \pm 0.03$  for our data (fitting the black hole mass dependence of  $\beta^{0.55} \propto r_0$ ). There are significant methodological differences between our results and those of Komiya et al. (2013): Komiya et al. (2013) measured black hole mass over a significantly broader redshift range ( $0.1 < z < 1.0$ ), used masses from three virial mass indicators (MgII, H $\beta$ , and H $\alpha$ ), and did not correct for differing redshift distributions between different bins in black hole mass, although they found only minor differences using reselected bins containing identical redshift distributions. We also note that other studies failed to find a significant relationship between black hole mass and clustering strength: Shen et al. (2009) found no dependence of quasar clustering on virial mass using

two bins in virial mass at  $0.4 < z < 2.5$ , and Zhang et al. (2013) found a 1–2  $\sigma$  difference in clustering strength between two bins in virial mass at  $0.6 < z < 1.2$ . Furthermore, Chatterjee et al. (2013) found no significant relationship between host cluster mass and virial mass at  $0.1 < z < 0.3$ ; rather than using clustering to measure the linear bias, they directly matched quasars with galaxy clusters and estimated the cluster mass using the optical richness.

Our results also appear to conflict with the predictions of many different models, which predict a relationship between black hole mass and host halo mass (Lidz et al. 2006, Kauffmann & Haehnelt 2002, Conroy & White 2013, Ferrarese 2002). These models all predict  $M_{\text{BH}} \propto M_{\text{DMH}}^\alpha$  over the range of masses considered here, with  $1.2 < \alpha < 1.8$ . We compare our data to these predictions by estimating the  $\beta$ -black hole mass relationship that would result from these  $M_{\text{BH}} - M_{\text{DMH}}$  relationships.

We begin by relating  $M_{\text{DMH}}$  to the linear quasar bias  $b_Q$ . We use the fitting formula of Sheth et al. (2001) to find  $b(M)$ :

$$b = 1 + \frac{1}{\sqrt{a}\delta_{sc}(z)} \left[ \frac{\sqrt{a}(a\nu^2) + \sqrt{ab}(a\nu^2)^{1-c}}{(a\nu^2)^c + b(1-c)(1-c/2)} \right] \quad (15)$$

where  $a = 0.707$ ,  $b = 0.5$ ,  $c = 0.6$ ,  $\nu = \delta_{sc}(z)/\sigma(M, z)$  and  $\delta_{sc}(z) = 0.15(12\pi)^{2/3}\Omega_m^{0.0055}$  (Navarro et al. 1997).  $\sigma(M, z) = \sigma(M, z=0)D(z)$ , where  $D(z)$  is the linear growth factor. We approximate  $D(z)$  using the fitting form of Carroll et al. (1992):

$$D(z) = \frac{D_1(z)}{D_1(0)}$$

$$D_1(z) = \left( \frac{1}{1+z} \right) \frac{5}{2} \Omega_{mz} \left[ \Omega_{mz}^{4/7} - \Omega_{\Lambda z} + \left( 1 + \frac{\Omega_{mz}}{2} \right) \left( 1 + \frac{\Omega_{\Lambda z}}{70} \right) \right]^{-1} \quad (16)$$

where  $\Omega_{mz}$  and  $\Omega_{\Lambda z}$  give the evolution of the cosmological parameters  $\Omega_m$  and  $\Omega_\Lambda$ .  $\sigma(M, z=0)$  is the fluctuation in the density field for a halo of mass  $M$  at redshift 0, given by

$$\sigma^2(r) = \frac{1}{2\pi^2} \int_0^\infty k^2 P(k) W^2(kr) dk \quad (17)$$

where  $P(k)$  is the power spectrum of the linear-regime matter field, computed from the transfer function of Eisenstein & Hu (1998),

$$W(kr) = \frac{3[\sin kr - kr \cos kr]}{(kr)^3} \quad (18)$$

and  $r(M) = (3M/(4\pi\rho_0))^{1/3}$ , where  $\rho_0$  is the mean density of the Universe at  $z = 0$ ,  $2.78 \times 10^{11} \Omega_m h^2 M_\odot \text{Mpc}^{-3}$ . We normalize the linear power spectrum such that  $\sigma(r = 8h^{-1} \text{Mpc}) = 0.84$ .

Since our angular clustering measurement does not allow for accurate estimates of  $b_Q$ , we relate  $b_Q$  to  $\beta$  using previous measurements of  $b_Q$  at  $z = 0.8$ . Croom

et al. (2005) measured  $b_Q(z = 0.8) = 1.49 \pm 0.21$ ; they also provided an empirical quadratic fit to their measurements of  $b_Q$  from  $z = 0.53$  to  $z = 2.48$ , yielding  $b_Q(z = 0.8) = 1.47 \pm 0.2$ . We fit a quadratic function to the measurements of Shen et al. (2009, 2013), White et al. (2012), Padmanabhan et al. (2009), Croom et al. (2005), Porciani & Norberg (2006), using 29 different measurements with  $0.3 < z < 3.8$  and obtain  $b_Q(z = 0.8) = 1.43$ . Following these estimates, we use  $b_Q = 1.5$  as the linear bias of our sample. Since  $b_Q \propto \beta$ , we multiply  $b(M)$  by the ratio between  $\beta = 0.105$  and  $b(z = 0.8) = 1.5$ . Since  $b(M)$  is approximately linear over 1 decade in host halo mass,  $\beta(M_{\text{BH}})$  is well-approximated by a power law.

The power-law slopes  $1.2 < d \log M_{\text{BH}} / d \log M_{\text{DMH}} < 1.8$  correspond to  $0.1 < d \log \beta / d \log M_{\text{BH}} < 0.15$ . We only find  $\approx 1\sigma$  difference between these slopes and our measurement of the MgII virial mass dependence of clustering, after adjusting for the factor of 1.5–2 suppression arising from the large scatter in the virial masses. Our results are also consistent with no relationship between  $M_{\text{BH}}$  and  $M_{\text{DMH}}$ , a possibility suggested by Shanks et al. (2011), who argue that the lack of luminosity-dependent clustering and the corresponding long quasar lifetime supports a pure luminosity evolution model, in which bright quasars at high redshift become faint Seyfert galaxies at  $z = 0$ . In the pure luminosity evolution model, host halo mass is not tightly related to black hole mass, as supported by the results of Kormendy et al. (2011) and Kormendy & Bender (2011), who found no relationship between black hole mass and stellar disk mass in disk galaxies at  $z = 0$ . Our results suggest that discriminating between models with no link between black hole mass and host halo mass and models with a tight relationship between black hole mass and host halo mass will require clustering measurements with larger samples and larger dynamic range in black hole mass.

## 6. CONCLUSIONS

Measuring the luminosity dependence of the quasar clustering amplitude allows us to test different relationships between host halo mass and quasar luminosity. Previous measurements of the quasar autocorrelation function and the three-dimensional quasar-galaxy cross-correlation function have suffered from small sample sizes: the spatial density of quasars is low, and it is difficult to obtain a large number of spectroscopic redshifts distributed across the sky. This study alleviates these concerns by measuring the angular overdensity between galaxies and quasars, resulting in a much higher density of the tracer population.

We find no luminosity dependence of the quasar-galaxy cross-correlation function, consistent with previous findings. A power law fit of luminosity to clustering amplitudes gives a slope of  $-0.01 \pm 0.06$ , a much tighter constraint than those provided by previous studies at similar redshift. We also fail to detect a relationship between clustering strength and MgII-based virial black hole mass. However, this result is consistent with theoretical predictions tightly linking black hole mass and host halo mass. These results indicate that, within the ranges of luminosities considered here, the most luminous quasars reside in a wide range of dark matter halos.

## 7. ACKNOWLEDGMENTS

We thank Doug Finkbeiner, Yue Shen, Adam Myers, Martin White, and Lars Hernquist for helpful comments and suggestions. We also thank Aaron Bray and Mario Juric for assistance with the SDSS imaging mask and the selection queries for the WISE and SDSS galaxies, respectively. A.G.K. acknowledges support from the Harvard College Research Program.

This publication makes use of data products from the Wide-field Infrared Survey Explorer, which is a joint project of the University of California, Los Angeles, and the Jet Propulsion Laboratory/California Institute of Technology, funded by the National Aeronautics and Space Administration.

Funding for SDSS-III has been provided by the Alfred P. Sloan Foundation, the Participating Institutions, the National Science Foundation, and the U.S. Department of Energy Office of Science. The SDSS-III web site is <http://www.sdss3.org/>. SDSS-III is managed by the Astrophysical Research Consortium for the Participating Institutions of the SDSS-III Collaboration including the University of Arizona, the Brazilian Participation Group, Brookhaven National Laboratory, Carnegie Mellon University, University of Florida, the French Participation Group, the German Participation Group, Harvard University, the Instituto de Astrofísica de Canarias, the Michigan State/Notre Dame/JINA Participation Group, Johns Hopkins University, Lawrence Berkeley National Laboratory, Max Planck Institute for Astrophysics, Max Planck Institute for Extraterrestrial Physics, New Mexico State University, New York University, Ohio State University, Pennsylvania State University, University of Portsmouth, Princeton University, the Spanish Participation Group, University of Tokyo, University of Utah, Vanderbilt University, University of Virginia, University of Washington, and Yale University.

## REFERENCES

- Adelberger, K. L., & Steidel, C. C. 2005, *ApJ*, 630, 50  
Aihara, H., Allende Prieto, C., An, D., et al. 2011a, *ApJS*, 195, 26  
—, 2011b, *ApJS*, 193, 29  
Blanton, M. R., Lin, H., Lupton, R. H., et al. 2003, *AJ*, 125, 2276  
Blanton, M. R., Schlegel, D. J., Strauss, M. A., et al. 2005, *AJ*, 129, 2562  
Bolton, A. S., Schlegel, D. J., Aubourg, É., et al. 2012, *AJ*, 144, 144  
Bonoli, S., Marulli, F., Springel, V., et al. 2009, *MNRAS*, 396, 423  
Booth, C. M., & Schaye, J. 2010, *MNRAS*, 405, L1  
Bovy, J., Hennawi, J. F., Hogg, D. W., et al. 2011, *ApJ*, 729, 141  
Carroll, S. M., Press, W. H., & Turner, E. L. 1992, *ARA&A*, 30, 499  
Chatterjee, S., Degraf, C., Richardson, J., et al. 2012, *MNRAS*, 419, 2657  
Chatterjee, S., Nguyen, M. L., Myers, A. D., & Zheng, Z. 2013, *ApJ*, 779, 147  
Coil, A. L., Hennawi, J. F., Newman, J. A., Cooper, M. C., & Davis, M. 2007, *ApJ*, 654, 115  
Cole, S., & Kaiser, N. 1989, *MNRAS*, 237, 1127  
Conroy, C., & White, M. 2013, *ApJ*, 762, 70  
Croom, S. M., Smith, R. J., Boyle, B. J., et al. 2004, *MNRAS*, 349, 1397  
Croom, S. M., Boyle, B. J., Shanks, T., et al. 2005, *MNRAS*, 356, 415  
Croton, D. J. 2009, *MNRAS*, 394, 1109  
da Ángela, J., Shanks, T., Croom, S. M., et al. 2008, *MNRAS*, 383, 565  
Dawson, K. S., Schlegel, D. J., Ahn, C. P., et al. 2013, *AJ*, 145, 10  
Degraf, C., Di Matteo, T., & Springel, V. 2011, *MNRAS*, 413, 1383  
Di Matteo, T., Springel, V., & Hernquist, L. 2005, *Nature*, 433, 604  
Eisenstein, D. J., & Hu, W. 1998, *ApJ*, 496, 605  
Eisenstein, D. J., Weinberg, D. H., Agol, E., et al. 2011, *AJ*, 142, 72  
Fanidakis, N., Baugh, C. M., Benson, A. J., et al. 2012, *MNRAS*, 419, 2797  
Ferrarese, L. 2002, *ApJ*, 578, 90  
Ferrarese, L., & Merritt, D. 2000, *ApJ*, 539, L9  
Fine, S., Croom, S. M., Miller, L., et al. 2006, *MNRAS*, 373, 613  
Fukugita, M., Ichikawa, T., Gunn, J. E., et al. 1996, *AJ*, 111, 1748  
Fukugita, M., Yasuda, N., Brinkmann, J., et al. 2004, *AJ*, 127, 3155  
Gebhardt, K., Bender, R., Bower, G., et al. 2000, *ApJ*, 539, L13  
Górski, K. M., Hivon, E., Banday, A. J., et al. 2005, *ApJ*, 622, 799  
Gunn, J. E., Carr, M., Rockosi, C., et al. 1998, *AJ*, 116, 3040  
Gunn, J. E., Siegmund, W. A., Mannery, E. J., et al. 2006, *AJ*, 131, 2332  
Haiman, Z., & Hui, L. 2001, *ApJ*, 547, 27  
Hickox, R. C., Jones, C., Forman, W. R., et al. 2009, *ApJ*, 696, 891  
Ho, S., Cuesta, A., Seo, H.-J., et al. 2012, *ApJ*, 761, 14  
Hogg, D. W., Finkbeiner, D. P., Schlegel, D. J., & Gunn, J. E. 2001, *AJ*, 122, 2129  
Hopkins, P. F., Hernquist, L., Cox, T. J., et al. 2005, *ApJ*, 630, 716  
—, 2006, *ApJS*, 163, 1  
Hopkins, P. F., Hernquist, L., Cox, T. J., & Kereš, D. 2008, *ApJS*, 175, 356  
Hopkins, P. F., Kocevski, D. D., & Bundy, K. 2014, *MNRAS*, 445, 823  
Hopkins, P. F., Lidz, A., Hernquist, L., et al. 2007, *ApJ*, 662, 110  
Ivezić, Ž., Lupton, R. H., Schlegel, D., et al. 2004, *Astronomische Nachrichten*, 325, 583  
Kaspi, S., Smith, P. S., Netzer, H., et al. 2000, *ApJ*, 533, 631  
Kauffmann, G., & Haehnelt, M. 2000, *MNRAS*, 311, 576  
Kauffmann, G., & Haehnelt, M. G. 2002, *MNRAS*, 332, 529  
Kochanek, C. S., Eisenstein, D. J., Cool, R. J., et al. 2012, *ApJS*, 200, 8  
Kollmeier, J. A., Onken, C. A., Kochanek, C. S., et al. 2006, *ApJ*, 648, 128  
Komiya, Y., Shirasaki, Y., Ohishi, M., & Mizumoto, Y. 2013, *ApJ*, 775, 43  
Kormendy, J., & Bender, R. 2011, *Nature*, 469, 377  
Kormendy, J., Bender, R., & Cornell, M. E. 2011, *Nature*, 469, 374  
Kormendy, J., & Richstone, D. 1995, *ARA&A*, 33, 581  
Krumpe, M., Miyaji, T., Coil, A. L., & Aceves, H. 2012, *ApJ*, 746, 1  
Lidz, A., Hopkins, P. F., Cox, T. J., Hernquist, L., & Robertson, B. 2006, *ApJ*, 641, 41  
Lupton, R. H., Gunn, J. E., & Szalay, A. S. 1999, *AJ*, 118, 1406  
Magorrian, J., Tremaine, S., Richstone, D., et al. 1998, *AJ*, 115, 2285  
Marconi, A., & Hunt, L. K. 2003, *ApJ*, 589, L21  
Martini, P., & Weinberg, D. H. 2001, *ApJ*, 547, 12  
Ménard, B., Scranton, R., Fukugita, M., & Richards, G. 2010, *MNRAS*, 405, 1025  
Mo, H. J., & White, S. D. M. 1996, *MNRAS*, 282, 347  
Mountrichas, G., Sawangwit, U., Shanks, T., et al. 2009, *MNRAS*, 394, 2050  
Myers, A. D., Brunner, R. J., Nichol, R. C., et al. 2007, *ApJ*, 658, 85  
Myers, A. D., Outram, P. J., Shanks, T., et al. 2003, *MNRAS*, 342, 467  
—, 2005, *MNRAS*, 359, 741  
Navarro, J. F., Frenk, C. S., & White, S. D. M. 1997, *ApJ*, 490, 493  
Padmanabhan, N., White, M., Norberg, P., & Porciani, C. 2009, *MNRAS*, 397, 1862  
Padmanabhan, N., Schlegel, D. J., Finkbeiner, D. P., et al. 2008, *ApJ*, 674, 1217  
Pâris, I., Petitjean, P., Aubourg, É., et al. 2014, *A&A*, 563, A54  
Pier, J. R., Munn, J. A., Hindsley, R. B., et al. 2003, *AJ*, 125, 1559  
Porciani, C., & Norberg, P. 2006, *MNRAS*, 371, 1824  
Press, W. H., & Schechter, P. 1974, *ApJ*, 187, 425

- Richards, G. T., Fan, X., Newberg, H. J., et al. 2002, *AJ*, 123, 2945
- Richards, G. T., Strauss, M. A., Fan, X., et al. 2006, *AJ*, 131, 2766
- Ross, A. J., Ho, S., Cuesta, A. J., et al. 2011, *MNRAS*, 417, 1350
- Schlegel, D. J., Finkbeiner, D. P., & Davis, M. 1998, *ApJ*, 500, 525
- Schneider, D. P., Richards, G. T., Hall, P. B., et al. 2010, *AJ*, 139, 2360
- Scranton, R., Johnston, D., Dodelson, S., et al. 2002, *ApJ*, 579, 48
- Scranton, R., Ménard, B., Richards, G. T., et al. 2005, *ApJ*, 633, 589
- Shankar, F., Weinberg, D. H., & Shen, Y. 2010, *MNRAS*, 406, 1959
- Shanks, T., Croom, S. M., Fine, S., Ross, N. P., & Sawangwit, U. 2011, *MNRAS*, 416, 650
- Shen, Y. 2009, *ApJ*, 704, 89
- . 2013, *Bulletin of the Astronomical Society of India*, 41, 61
- Shen, Y., Greene, J. E., Strauss, M. A., Richards, G. T., & Schneider, D. P. 2008, *ApJ*, 680, 169
- Shen, Y., & Kelly, B. C. 2012, *ApJ*, 746, 169
- Shen, Y., & Liu, X. 2012, *ApJ*, 753, 125
- Shen, Y., Strauss, M. A., Ross, N. P., et al. 2009, *ApJ*, 697, 1656
- Shen, Y., Richards, G. T., Strauss, M. A., et al. 2011, *ApJS*, 194, 45
- Shen, Y., McBride, C. K., White, M., et al. 2013, *ApJ*, 778, 98
- Sheth, R. K., Mo, H. J., & Tormen, G. 2001, *MNRAS*, 323, 1
- Shirasaki, Y., Tanaka, M., Ohishi, M., et al. 2011, *PASJ*, 63, 469
- Silk, J., & Rees, M. J. 1998, *A&A*, 331, L1
- Smee, S. A., Gunn, J. E., Uomoto, A., et al. 2013, *AJ*, 146, 32
- Smith, J. A., Tucker, D. L., Kent, S., et al. 2002, *AJ*, 123, 2121
- Soltan, A. 1982, *MNRAS*, 200, 115
- Spiegel, D. N., Verde, L., Peiris, H. V., et al. 2003, *ApJS*, 148, 175
- Stoughton, C., Lupton, R. H., Bernardi, M., et al. 2002, *AJ*, 123, 485
- Thacker, R. J., Scannapieco, E., Couchman, H. M. P., & Richardson, M. 2009, *ApJ*, 693, 552
- Tucker, D. L., Kent, S., Richmond, M. W., et al. 2006, *Astronomische Nachrichten*, 327, 821
- Vestergaard, M., & Peterson, B. M. 2006, *ApJ*, 641, 689
- White, M., Blanton, M., Bolton, A., et al. 2011, *ApJ*, 728, 126
- White, M., Myers, A. D., Ross, N. P., et al. 2012, *MNRAS*, 424, 933
- Wright, E. L., Eisenhardt, P. R. M., Mainzer, A. K., et al. 2010, *AJ*, 140, 1868
- Yee, H. K. C., & Green, R. F. 1987, *ApJ*, 319, 28
- York, D. G., Adelman, J., Anderson, Jr., J. E., et al. 2000, *AJ*, 120, 1579
- Zehavi, I., Zheng, Z., Weinberg, D. H., et al. 2011, *ApJ*, 736, 59
- Zhang, S., Wang, T., Wang, H., & Zhou, H. 2013, *ApJ*, 773, 175